# 9 SCIENTIFIC HIGHLIGHT OF THE MONTH: Calculating Scattering Matrices by Wave Function Matching

---

## Calculating Scattering Matrices by Wave Function Matching

G. Brocks, V. M. Karpan, P. J. Kelly, P. A. Khomyakov, I. Marushchenko, A. Starikov, M. Talanana, I. Turek,[1] K. Xia,[2] P. X. Xu, M. Zwierzycki[3], G. E. W. Bauer[4]

Faculty of Science and Technology and MESA+ Institute for Nanotechnology,
University of Twente, P. O. Box 217, 7500 AE Enschede, The Netherlands

[1]Institute of Physics of Materials, Academy of Sciences of the Czech Republic, CZ-616 62 Brno, Czech Republic

[2]Beijing National Laboratory for Condensed Matter Physics, Institute of Physics, Chinese Academy of Sciences, Beijing 100080, China

[3]Institute of Molecular Physics, P.A.N., Smoluchowskiego 17, 60-179 Poznań, Poland.

[4]Kavli Institute of NanoScience, Delft University of Technology, Lorentzweg 1, 2628 CJ Delft, The Netherlands.

### Abstract

As devices are reduced in size, interfaces start to dominate electrical transport making it essential to be able to describe reliably how they transmit and reflect electrons. Wave function matching (WFM) is a transparent technique for calculating transmission and reflection matrices suitable for any Hamiltonian that can be represented in tight-binding form. A first-principles Kohn-Sham Hamiltonian represented on a localized orbital basis or on a real space grid has such a form. WFM is based upon direct matching of the scattering-region wave function to the Bloch modes of the leads. In this paper we give a pedagogical introduction to WFM. We briefly discuss WFM for calculating the conductance of atomic wires, using a real space grid implementation. A tight-binding muffin-tin orbital implementation very suitable for studying spin-dependent transport in layered magnetic materials is illustrated by looking at spin-dependent transmission through ideal and disordered interfaces.

## 1 Calculating the scattering matrix from first principles

Various methods have been developed for calculating the transmission of electrons through an interface (or a more extended scattering region) from first principles [1–15], or using as input electronic structures which were calculated from first principles [16–22]. Most are based upon a formulation for the conductance in terms of non-equilibrium Green's functions (NEGF) [23] which reduces in the appropriate limit to the well known Fisher-Lee linear-response form [24] for the conductance of a finite disordered wire embedded between crystalline leads. An alternative technique, suitable for Hamiltonians that can be represented in tight-binding form, has been formulated by Ando [25] and is based upon direct matching of the scattering-region wave function to the Bloch modes of the leads[1]. A third approach based upon "embedding" [28,29] has been combined with full-potential linearized augmented plane wave method to yield what is probably the most accurate scheme to date [11,12] but is numerically very demanding.

Our main purpose is to outline a scheme suitable for studying microscopic transport in the linear response regime in inhomogeneous, mainly layered, materials which is physically transparent and first-principles, i.e., requiring no free parameters. Landauer and Büttiker formulated the problem of electronic transport in terms of scattering matrices where the transmission matrix element $t_{n,m}$ is the probability amplitude that a state $|n\rangle$ in the left-hand lead incident on the scattering region from the left (see Fig. 1) is scattered into a state $|m\rangle$ in the right-hand lead. The conductance $G = dI/dV|_{V=0}$ in the linear response regime is given by

$$G = \frac{e^2}{h} \sum_{n,m} |t_{n,m}|^2. \tag{1}$$

The Landauer-Büttiker approach is intuitively very appealing because wave transport through interfaces is so naturally described in terms of transmission and reflection. Usually, explicit calculation of the scattering states is avoided by making use of the invariance properties of the trace in Eq. 1 to calculate the conductance directly from Green functions expressed in some convenient localized orbital representation [23]. However, we want to make contact with the large body of theoretical literature on mesoscopic physics [30,31] which requires calculation of the full microscopic transmission and reflection matrices and make use of the explicit knowledge of the scattering states to analyze our numerical results. Our requirement of physical transparency is satisfied by choosing a computational scheme which yields the full scattering matrix and not just the conductance.

Any workable first-principles scheme is at present based upon an independent particle approximation. An extremely successful framework for calculating ground state properties of a wide variety of materials is Density Functional Theory (DFT) using functionals based upon the Local Density Approximation (LDA) or the Generalized Gradient Approximation (GGA). DFT/LDA or GGA calculations and their spin-polarized versions yield a charge (spin) density in all space as well as a Kohn-Sham effective potential. We assume that the latter can be used in describing the electron transport within the Landauer-Büttiker formalism in the linear response regime. This then satisfies our requirement of introducing no free parameters.

To calculate transmission and reflection matrices from first principles, we combined the wave-function matching (WFM) formalism described by Ando [25] for an empirical tight-binding Hamiltonian, with an ab-initio tight-binding Hamiltonian. A version of this method has been implemented for a real-space grid, using a high order finite difference scheme. It has been applied to the calculation of the conductance of atomic wires [15,32]. Another implementation is based upon a representation on an ab-initio TB-MTO basis [7,33,34]. The method which results, was applied to a number of problems of current interest in spin-transport: to the calculation of spin-dependent interface resistances where interface disorder was modeled by means of large lateral supercells [7,35]; to the first principles calculation of the spin mixing conductance parameter entering theories with non-collinear magnetizations, relevant for the spin-transfer torque [36] and the related problem of Gilbert damping enhancement in the presence of interfaces [37]; to a generalized scattering formulation of the suppression of Andreev scattering at a ferromagnetic|superconducting interface [38]; to the problem of how spin-dependent interface resistances influence spin injection from a metallic ferromagnet into a III–V semiconductor [39–41] and to the influence of roughness and disorder on tunneling magnetoresistance [42].

In this section we give a general exposé of the wave-function matching method. In Sec. 2 we will discuss an application to atomic wires based upon a real space grid implementation. Applications to (magnetic)

---

[1] The relationship between the wave function matching (WFM) [25] and Green function [23,24] approaches is not immediately obvious. It was suggested recently that WFM was incomplete [26] but the complete equivalence of the two approaches could be proven [27].

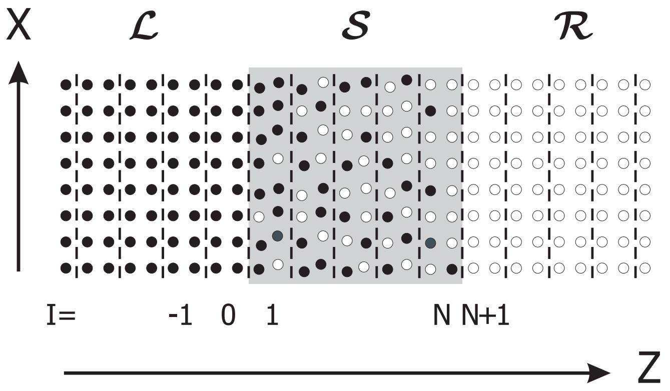

Figure 1: Sketch of the configuration used in the Landauer-Büttiker transport formulation to calculate the two terminal conductance. A (shaded) scattering region ($\mathcal{S}$) is sandwiched by left- ($\mathcal{L}$) and right-hand ($\mathcal{R}$) leads which have translational symmetry and are partitioned into principal layers perpendicular to the transport direction. The scattering region contains $N$ principal layers but the structure and chemical composition are in principle arbitrary.

interfaces based upon a TB-MTO implementation are discussed in Sec. 3.

## 1.1 Formalism

In layered structures Bloch translational symmetry is broken so that the Kohn-Sham equations have to be solved for the infinite system represented by Fig. 1. This problem is reduced to finite size by replacing the semi-infinite leads by appropriate energy dependent boundary conditions as represented by Fig. 2. This can be achieved by the wave-function matching (WFM) method for calculating the transmission and reflection matrices due to Ando [25]. In the next sections we will give a very simple, pedagogical introduction to this method. We restrict ourselves to the linear response regime. The full details of the formalism and of the implementations can be found in Refs. [15, 27, 34]

### 1.1.1 Wave function matching in one dimension

The essence of WFM can be explained at an introductory quantum mechanics level. We start from Fig. 3, which represents a one-dimensional potential barrier with constant potentials in the leads (the left and right regions). We discretize the Schrödinger equation and approximate the second derivative by a first order finite difference expression.

$$E\psi_i + \frac{\hbar^2}{2m}\left\{\frac{(\psi_{i+1}-\psi_i)-(\psi_i-\psi_{i-1})}{\Delta^2}\right\} - V_i\psi_i = 0, \tag{2}$$

where $\psi_i$ and $V_i$ are shorthand notations for $\psi(x_i)$ and $V(x_i)$, and $\Delta = x_{i+1} - x_i$ (the grid is equidistant). In a scattering problem $i$ runs from $-\infty$ to $\infty$, leading to an infinite number of equations. This is awkward and unnecessary, since the scattering potential is localized in space, i.e. $V(x)$ differs from a constant only for $x_1 \leq x \leq x_N$. For the left and right regions, $x < x_1$ and $x > x_N$, the solutions to the Schrödinger equation are simple plane waves, see Fig. 3, with

$$k_L = \frac{\sqrt{2m(E-V_L)}}{\hbar}\ ;\ k_R = \frac{\sqrt{2m(E-V_R)}}{\hbar}. \tag{3}$$

To obtain a full solution of the Schrödinger equation, we only need to match these “modes” to the wave function in the region of the potential barrier (the scattering region).

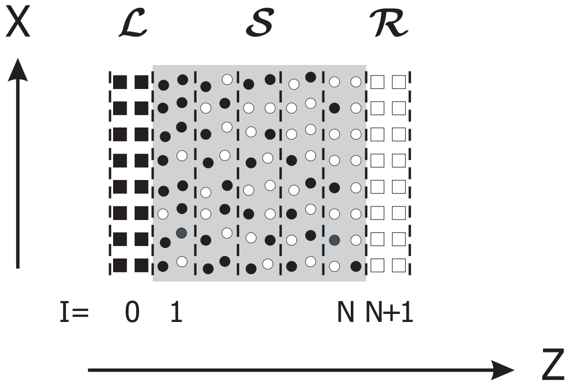

Figure 2: The semi-infinite leads and corresponding Hamiltonian problem with an infinite number of layers from Fig. 1 is replaced by finite leads and an effective Hamiltonian. The effective Hamiltonian is simply constructed by adding the energy-dependent self-energies $\Sigma_{\mathcal{L}}$ and $\Sigma_{\mathcal{R}}$ to the $\mathcal{H}_{0,0}$ and $\mathcal{H}_{N+1,N+1}$ Hamiltonian blocks, respectively, where the indices are principal layer indices. The lead atoms modified by the self energy are depicted as squares. The left and right self-energies are constructed in terms of generalized Bloch matrices and blocks of lead hopping matrices for the left-hand and right-hand leads, respectively.

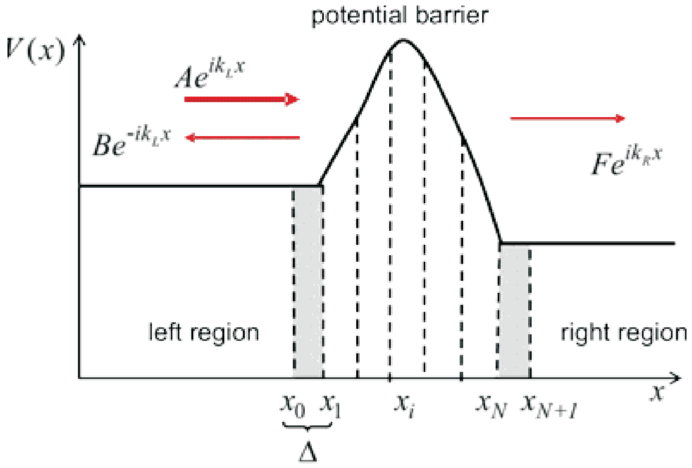

Figure 3: Discretization of a potential barrier. An equidistant grid is applied with $\Delta = x_{i+1} - x_i$. The potential is different from a constant for $x_1 \leq x \leq x_N$. The coupling to the left and right regions (the leads) can be included by extending the grid by two points, which defines the boundary zones, indicated in gray.

The finite difference Schrödinger equation for $i = 0$ is

$$E\psi_0 + \frac{\hbar^2}{2m\Delta^2}\left\{\psi_1 - 2\psi_0 + \psi_{-1}\right\} - V_0\psi_0 = 0. \tag{4}$$

We set $x_0 = 0$. For $x < 0$ the wave function has the form $\psi(x) = Ae^{ik_L x} + Be^{-ik_L x}$, so

$$\psi_{-1} = Ae^{-ik_L\Delta} + Be^{ik_L\Delta} = Ae^{-ik_L\Delta} + (\psi_0 - A)\, e^{ik_L\Delta}, \tag{5}$$

since the wave function is continuous at $x = 0$. In a scattering problem we assume that we have set the incoming wave, so $A$ is fixed. Eq. 4 is rewritten as

$$E\psi_0 + \frac{\hbar^2}{2m\Delta^2}\left\{\psi_1 - 2\psi_0 + e^{ik_L\Delta}\psi_0\right\} - V_0\psi_0 = \frac{\hbar^2}{2m\Delta^2}A\left\{e^{ik_L\Delta} - e^{-ik_L\Delta}\right\}. \tag{6}$$

The term on the left-hand side only contains $\psi_i$ with $i \geq 0$, and the terms on the right-hand side can be considered as a source term. This manipulation takes care of the left boundary.

For the right boundary we use a similar trick. For $i = N + 1$ we have

$$E\psi_{N+1} + \frac{\hbar^2}{2m\Delta^2}\left\{\psi_{N+2} - 2\psi_{N+1} + \psi_N\right\} - V_{N+1}\psi_{N+1} = 0. \tag{7}$$

Using

$$\psi_{N+2} = Fe^{ik_R(N+2)\Delta} = \psi_{N+1}e^{ik_R\Delta} \tag{8}$$

one obtains

$$E\psi_{N+1} + \frac{\hbar^2}{2m\Delta^2}\left\{\psi_{N+1}e^{ik_R\Delta} - 2\psi_{N+1} + \psi_N\right\} - V_{N+1}\psi_{N+1} = 0. \tag{9}$$

In Eq. 8 we have assumed only a transmitted wave on the right and no incoming wave. The term on the left-hand side of Eq. 9 contains only $\psi_i$ with $i \leq N + 1$. This manipulation takes care of the right boundary.

For $i = 1, \ldots, N$ we use Eq. 2 in unaltered form. Collecting Eqs. 2, 6 and 9 the scattering problem can be written as

$$\left(E\mathbf{I} - \mathbf{H}'\right)\boldsymbol{\psi} = \mathbf{q}. \tag{10}$$

Here $\boldsymbol{\psi}$ is a vector containing the coefficients $\psi_i$; $i = 0, \ldots, N + 1$; $\mathbf{q}$ is the "source" vector of length $N + 2$. Only its first coefficient is nonzero

$$q_0 = \frac{\hbar^2}{2m\Delta^2}A\left\{e^{ik\Delta} - e^{-ik\Delta}\right\}. \tag{11}$$

$\mathbf{H}'$ is the $(N + 2) \times (N + 2)$ Hamiltonian matrix. It is tridiagonal with most of its elements identical to those of the original finite difference Hamiltonian

$$H'_{i,i+1} = H'_{i,i-1} = -\frac{\hbar^2}{2m\Delta^2}, \tag{12}$$

$$H'_{i,i} = -\frac{\hbar^2}{m\Delta^2} + V_i, \tag{13}$$

except for the first and the last diagonal elements, which are modified to

$$\begin{aligned} H'_{0,0} &= -\frac{\hbar^2}{m\Delta^2} + V_0 + \Sigma_L(E), \\ H'_{N+1,N+1} &= -\frac{\hbar^2}{m\Delta^2} + V_{N+1} + \Sigma_R(E), \end{aligned} \tag{14}$$

with

$$\begin{aligned} \Sigma_L(E) &= -\frac{\hbar^2}{2m\Delta^2}e^{ik_L\Delta}, \\ \Sigma_R(E) &= -\frac{\hbar^2}{2m\Delta^2}e^{ik_R\Delta}. \end{aligned} \tag{15}$$

In Green function jargon $\Sigma_{L/R}(E)$ are called the self-energies of the left and right leads. They take care of the coupling of the potential barrier to the outer regions, and contain all the required information about the outer regions. The self-energy depends upon the energy of the incoming and scattered waves through Eq. 3. Whereas Eq. 2 represents an infinite dimensional problem, we have reduced it to a finite, $N+2$ dimensional problem, Eq. 10. It can be solved using standard algorithms for solving linear equations, such as Gaussian elimination. In this case it is particularly simple, since the matrix is tridiagonal.

Once Eq. 10 is solved, it remains to extract the transmission and reflection amplitudes. The transmission amplitude is given by the wave function on the right side of the barrier, normalized to the amplitude of the incoming wave, and (flux) normalized with the velocities to obtain a unitary scattering matrix [43]

$$t = \sqrt{\frac{v_R}{v_L}} \frac{\psi_{N+1}}{A}. \tag{16}$$

The reflection amplitude is similarly determined from the wave function on the left side minus the incoming wave, normalized to the incoming wave

$$r = \frac{\psi_0 - A}{A}. \tag{17}$$

Some care should be taken in determining the velocities. Since we have discretized the Schrödinger equation, it is consistent to discretize the expression for the current in a similar way

$$J = \frac{i\hbar}{2m}\left(\psi_i \frac{\psi^*_{i+1} - \psi^*_i}{\Delta} - \psi^*_i \frac{\psi_{i+1} - \psi_i}{\Delta}\right). \tag{18}$$

For a simple plane wave $Ae^{ikx}$ this expression gives

$$J = \frac{i\hbar \left|A\right|^2}{2m\Delta}\left(e^{-ik\Delta} - e^{ik\Delta}\right),$$

Since $J$ is particle density $\left|A\right|^2$ times velocity $v$, one obtains

$$v = \frac{i\hbar}{2m\Delta}\left(e^{-ik\Delta} - e^{ik\Delta}\right). \tag{19}$$

The source term, Eq. 11, can then be simplified to

$$q_0 = \frac{i\hbar A}{\Delta} v_L. \tag{20}$$

From Eqs. 19 and 15 one can relate the velocity to the self-energy

$$v_{L/R} = -\frac{2\Delta}{\hbar} \operatorname{Im} \Sigma_{L/R}(E). \tag{21}$$

### Green function expressions

Using Green functions these results can be put into a very compact, albeit somewhat obscure, form. One can define a Green function matrix by

$$\mathbf{G}(E) = \left(E\mathbf{I} - \mathbf{H}'\right)^{-1}. \tag{22}$$

It has dimensions $N+2$, like the modified Hamiltonian matrix $\mathbf{H}'$. One can also define the infinite dimensional retarded Green function matrix related to the original infinite dimensional Hamiltonian

$$\mathbf{G}^r(E) = \left[(E + i\eta)\mathbf{I} - \mathbf{H}\right]^{-1}, \tag{23}$$

where $\eta$ is (real, positive) infinitesimal. For $z$ a complex number in the lower half plane, the matrix elements of $\mathbf{G}(z)$ and $\mathbf{G}^r(z)$ in the scattering region are identical [43]. Note that $\mathbf{H}'$ is non-Hermitian, because the self-energy $\Sigma$ is complex, see Eqs. 14 and 15. One can show that the eigenvalues of $\mathbf{H}'$ are

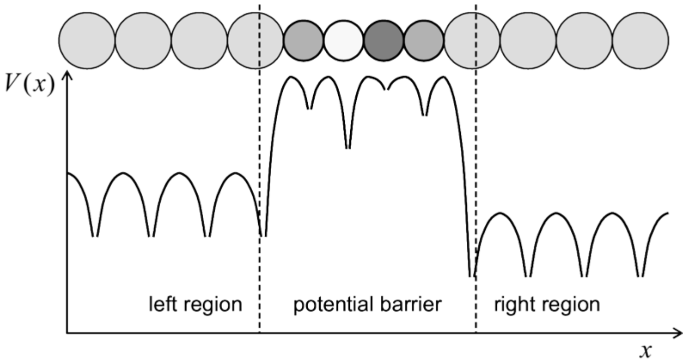

Figure 4: *Top*: atomic chain. The leads (left and right region) are periodic chains of identical atoms. The middle region contains different atoms and/or disorder. *Bottom*: schematic representation of the potential along the chain.

not real and lie in the upper half complex plane. Thus $\mathbf{G}(E)$ is a well-defined quantity for real energies $E$. By construction it has the retarded boundary condition build into it and one does not need the usual $+i\eta$ trick.

The definition of $\mathbf{G}$ allows us to write

$$\psi_{N+1} = G_{N+1,0}(E)q_0, \tag{24}$$

see Eq. 10. Eqs. 16, 20 and 24 then lead to a compact Fisher-Lee expression for the transmission amplitude [24]

$$t = \frac{i\hbar}{\Delta}\sqrt{v_R v_L}\, G_{N+1,0}(E), \tag{25}$$

which relates matrix elements of the scattering matrix to matrix elements of the Green function. Using Eq. 21 we can write

$$t = 2i\sqrt{-\operatorname{Im}\Sigma_R}\, G_{N+1,0}(E)\, \sqrt{-\operatorname{Im}\Sigma_L}, \tag{26}$$

which allows the transmission coefficient to be written as

$$T = t^* t = 4(\operatorname{Im}\Sigma_R)G^r_{N+1,0}(\operatorname{Im}\Sigma_L)G^a_{0,N+1}, \tag{27}$$

with all quantities evaluated at a fixed energy $E$, and $\mathbf{G}^a = [\mathbf{G}^r]^\dagger$ the advanced Green-function matrix. Eq. 27 is known as the Caroli expression [23]. Its generalization to finite bias, i.e. to the non-linear response regime, is also known as the non-equilibrium Green function or NEGF expression.

### 1.1.2 Tight binding

Wave function matching can be extended straightforwardly to LCAO (linear combinations of atomic orbitals) and tight-binding (TB: nearest-neighbour interactions only) Hamiltonians. We illustrate this in one dimension for the atomic wire sketched in Fig. 4.

In the LCAO approximation, wave functions are expanded in a basis set of fixed atomic orbitals $\psi(x) = \sum_i c_i \chi_i(x - X_i)$,where $X_i$ denote the positions of the atoms. The wave function is then represented by the column vector of the coefficients

$$\boldsymbol{\psi} = \begin{pmatrix} \vdots \\ c_{i-1} \\ c_i \\ c_{i+1} \\ \vdots \end{pmatrix}. \tag{28}$$

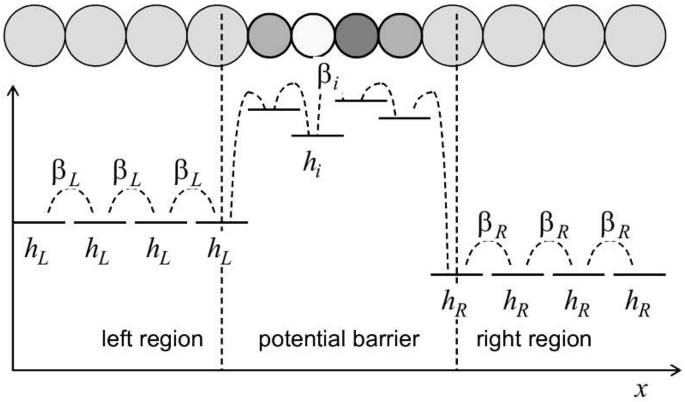

Figure 5: Nearest neighbor tight-binding model of an atomic chain. The periodic left and right regions are characterized by the on-site and hopping matrix elements $h_{L/R}$ and $\beta_{L/R}$. The scattering region has site dependent matrix elements $h_i$ and $\beta_i$.

Since we solve a scattering problem, the atomic orbitals cover all space, and the vector has infinite dimension, i.e. $i = -\infty, \ldots, \infty$. The Schrödinger equation becomes

$$(E\mathbf{I} - \mathbf{H})\,\boldsymbol{\psi} = \mathbf{0}, \tag{29}$$

with $\mathbf{H}$ the Hamiltonian matrix with matrix elements $H_{i,j} = \langle \chi_i | \widehat{H} | \chi_j \rangle$. To keep things simple we assume that the atomic orbital basis is orthonormal.[2] We use a single atomic orbital per site and we assume nearest neighbor interactions only (tight-binding). The diagonal elements of $\mathbf{H}$ are $H_{i,i} = h_i$; its off-diagonal elements are $H_{i+1,i} = \beta_i$, $H_{i,i+1} = \beta_i^*$ and all elements $H_{j,i} = 0$ for $j > i+1$ and $j < i-1$. The (Hermitian) Hamiltonian matrix is then

$$\mathbf{H} = \begin{pmatrix} \ddots & \cdots & 0 & 0 & \\ \vdots & h_{i-1} & \beta_{i-1}^* & 0 & 0 \\ 0 & \beta_{i-1} & h_i & \beta_i^* & 0 \\ 0 & 0 & \beta_i & h_{i+1} & \vdots \\ & 0 & 0 & \cdots & \ddots \end{pmatrix}. \tag{30}$$

None of these approximations is essential and the WFM formalism can be made to work for any LCAO representation; here we just want to keep the notation as simple as possible.

As before, we divide our system into three parts: a left lead, a scattering region, and a right lead. The left and right leads are crystalline materials with translational symmetry. Matrix elements in the leads must be site-independent, i.e. $h_i = h_{L/R}$ and $\beta_i = \beta_{L/R}$ for the left/right leads. Only in the scattering region do we have site-dependent matrix elements. The basic idea is illustrated in Fig. 5.

### Ideal lead modes

Writing out Eq. 29 in its components gives

$$-\beta_{i-1}c_{i-1} + (E - h_i)c_i - \beta_i^* c_{i+1} = 0, \tag{31}$$

with $i$ running from $-\infty$ to $\infty$. These equations have the same form as the discretized Schrödinger equation of Eq. 2 if we make the substitutions

$$c_i \to \psi_i \quad ; \quad h_i \to -\frac{\hbar^2}{m\Delta^2} + V_i \quad ; \quad \beta_i \to -\frac{\hbar^2}{2m\Delta^2}.$$

---

[2] For non-orthogonal basis sets one introduces an overlap matrix $\mathbf{S}$, with matrix elements $S_{i,j} = \langle \chi_i | \chi_j \rangle$, and replaces $\mathbf{I}$ by $\mathbf{S}$.

As before, the scattering problem is solved by WFM. First we have to find the modes of the ideal leads. For sites $i$ in the left lead the matrix elements are site independent and Eq. 31 becomes

$$-\beta_L c_{i-1} + (E - h_L)c_i - \beta_L^* c_{i+1} = 0. \tag{32}$$

This equation has the same form as a discretized Schrödinger equation for a particle in a constant potential, so the solutions are discretized plane waves, i.e.

$$c_n = Ae^{ik_L n a_L}, \tag{33}$$

where the distance between the atoms $a_L$ is the "discretization step". The same holds for the right lead, replacing the subscript $L$ by $R$.

One could derive this in a somewhat more formal way. As a consequence of the Bloch-Floquet theorem the functions in consecutive cells of a periodic system are related by a constant amplitude/phase factor $\lambda$, i.e.

$$\text{if } \; c_{i-1} = c \; \text{ then } \; c_i = \lambda c \; \text{ and } \; c_{i+1} = \lambda^2 c. \tag{34}$$

Assuming for simplicity that $\beta$ is real, Eq. 32 gives

$$\begin{aligned} -\beta + (E-h)\lambda - \beta\lambda^2 = 0 \Rightarrow \\ \lambda = \frac{E-h}{2\beta} \pm \left[\left(\frac{E-h}{2\beta}\right)^2 - 1\right]^{\frac{1}{2}}, \end{aligned} \tag{35}$$

where you add the subscript $L/R$ for the left and right leads. The roots $\lambda$ can be given a more familiar form. For $\left|\frac{E-h}{2\beta}\right| \leq 1$ we define a wave number $k$ by[3]

$$\cos(ka) = \frac{E-h}{2\beta}, \tag{36}$$

which leads to the simple form

$$\lambda_\pm = e^{\pm ika}, \tag{37}$$

i.e. the familiar form of the Bloch factor. Using Eq. 34 recursively, i.e. $c_n = \lambda^n c_0$, then leads to Eq. 33, with $A = c_0$. It describes propagating waves, with $\lambda_+$ a wave propagating to the right, and $\lambda_-$ a wave propagating to the left.

For $\left|\frac{E-h}{2\beta}\right| > 1$ one can define $\kappa$ by

$$\cosh(\kappa a) = \left|\frac{E-h}{2\beta}\right|, \tag{38}$$

and obtain

$$\begin{aligned} \lambda_\pm &= +e^{\mp\kappa a} \;\; \text{if} \;\; \frac{E-h}{2\beta} > 1; \\ \lambda_\pm &= -e^{\mp\kappa a} \;\; \text{if} \;\; \frac{E-h}{2\beta} < -1. \end{aligned} \tag{39}$$

Both these cases describe waves that decay either to the right or to the left, i.e. evanescent waves. They are not acceptable as solutions to the one-dimensional Schrödinger equation since one cannot normalize them. However, we have a use for them in three-dimensional problems, as we will see later on.

**Wave function matching**

Having obtained the modes of the ideal leads, we match them to the scattering region, where the matrix elements $h_i$ and $\beta_i$ in Eq. 31 are site dependent. We assume that the scattering region is localized in

---

[3] $E(k) = h + 2\beta\cos ka$ is of course the dispersion relation of a 1D $s$-band in the nearest neighbour tight-binding model.

space, so $i$ runs from 1 to $N$. The procedure we have used to solve the discretized Schrödinger problem in Sec. 1.1.1 can be copied with only small modifications. Using Eq. 37, Eqs. 5 and 8 read[4]

$$\begin{aligned} c_{-1} &= A\lambda_{L,+}^{-1} + B\lambda_{L,-}^{-1} = A\lambda_{L,+}^{-1} + (c_0 - A)\,\lambda_{L,-}^{-1}; \\ c_{N+2} &= c_{N+1}\lambda_{R,+}. \end{aligned} \tag{40}$$

Eq. 40 can be used to substitute Eq. 29 by

$$(E\mathbf{I} - \mathbf{H}')\,\boldsymbol{\psi} = \mathbf{q}, \tag{41}$$

similar to Eq. 10. $\boldsymbol{\psi}$ is a finite dimensional vector that contains the coefficients $c_i$ in the scattering region plus those in the two boundaries, i.e. $i = 0, \ldots, N+1$. $\mathbf{q}$ is the "source" vector of length $N+2$, whose coefficients are zero, except the first one

$$q_0 = \beta_L A \left\{ \lambda_{L,-}^{-1} - \lambda_{L,+}^{-1} \right\}. \tag{42}$$

$\mathbf{H}'$ is a finite $(N+2) \times (N+2)$ Hamiltonian matrix. All its matrix elements are identical to that of the original Hamiltonian matrix, Eq. 30, except for the first and the last diagonal element, which are modified to

$$\begin{aligned} H'_{0,0} &= h_0 + \Sigma_L(E); \\ H'_{N+1,N+1} &= h_{N+1} + \Sigma_R(E), \end{aligned} \tag{43}$$

with

$$\begin{aligned} \Sigma_L(E) &= \beta_L \lambda_{L,-}^{-1}; \\ \Sigma_R(E) &= \beta_R \lambda_{R,+}. \end{aligned} \tag{44}$$

These "self-energies" contain all the information concerning the coupling of the scattering region to the leads. As before, they are complex and energy dependent through Eqs. 36 and 37.

We have replaced an infinite dimensional problem, Eq. 29, by a finite dimensional one, Eq. 41. The latter has the same form as Eq. 10. Since "the same equations have the same solutions", the transmission amplitude of Eq. 16 becomes

$$t = \sqrt{\frac{v_R}{v_L}}\frac{c_{N+1}}{A} \tag{45}$$

with, as in Eq. 21, the velocities given by

$$v_{L/R} = -\frac{2a_{L/R}}{\hbar}\,\mathrm{Im}\,\Sigma_{L/R}(E). \tag{46}$$

Using WFM, simple scattering problems with tight-binding Hamiltonians can be solved analytically in a straightforward way, as illustrated in Refs. [27,32] The Green function expressions given in Sec. 1.1.1 are also valid for tight-binding Hamiltonians.

### 1.1.3 Wave function matching in three dimensions

In this section we generalize WFM to problems in three dimensions. We use Landauer's formula to express the conductance in terms of the transmission amplitudes $t_{n,m}$, see Eq. 1. We will see that calculating transmission amplitudes for scattering in layered systems in three dimensions is conceptually similar to the one-dimensional case.

---

[4] We write $c_{i+n} = \lambda_{\pm}^{n} c_i$, where $n$ is an integer (positive or negative), and let the ± indicate waves propagating to the left and right, respectively. In the one-dimensional case, one always has $\lambda_+ = 1/\lambda_-$. In the three-dimensional case, this relation does not necessarily hold. We use a notation that is easily generalized to three dimensions.

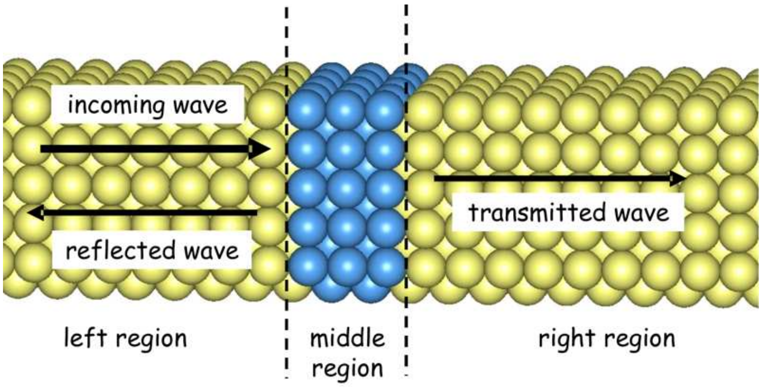

Figure 6: Schematic representation of a tunnel junction. The yellow balls represent atoms of a metal, the blue balls represent atoms of an insulator. The left and right regions stretch macroscopically far into the left and right, respectively. The electron waves in the metal are reflected or transmitted by the insulator in the middle region

As an example we consider the tunnel junction shown in Fig. 6. The principal idea is to divide the system into layers of atoms, normal to the transport direction. One chooses the layers sufficiently thick that the Hamiltonian matrix only contains matrix elements that either couple atoms within one layer, or atoms that are in nearest neighbor layers.[5] The Hamiltonian matrix of Eq. 30 becomes

$$\mathbf{H} = \begin{pmatrix} \ddots & \cdots & 0 & 0 & \\ \vdots & \mathbf{H}_{i-1} & \mathbf{B}_{i-1}^{\dagger} & 0 & 0 \\ 0 & \mathbf{B}_{i-1} & \mathbf{H}_{i} & \mathbf{B}_{i}^{\dagger} & 0 \\ 0 & 0 & \mathbf{B}_{i} & \mathbf{H}_{i+1} & \vdots \\ & 0 & 0 & \cdots & \ddots \end{pmatrix}, \tag{47}$$

with $i = -\infty, \ldots, \infty$. The matrices $\mathbf{H}_i$ contain the interactions between atoms within layer $i$, and $\mathbf{B}_i$ describe the coupling between layers $i$ and $i+1$. Both are $N \times N$ matrices, with $N$ the total number of atomic orbitals of all atoms in a layer. The scattering region is localized in the layers $i = 1, \ldots, S$. A schematic representation of the structure of the Hamiltonian is given Fig. 7.[6]

This representation is valid both for systems with a finite cross section (i.e. wires), and for infinite layered systems that are periodic along the interfaces. In the latter case $N$ refers to the number of atoms within the unit cell. $\mathbf{k}_{\parallel}$ is then a good quantum number and the matrices $\mathbf{H}_i(\mathbf{k}_{\parallel})$ depend on this quantum number. The exact forms of these matrices are not important here and to simplify the notation we will omit the quantum number $\mathbf{k}_{\parallel}$. Moreover, we will use the phrase "wire" to indicate both systems with a finite cross section and systems with infinite periodic interfaces.

---

[5] The formalism can be extended straightforwardly to include interactions of a longer range, but the notation becomes a bit messy, so we consider only nearest neighbour interactions here.

[6] Note that the notation has changed slightly here. Now $N$ is the dimension of the basis *within* one layer, and $S$ is the *number* of layers in the scattering region. Sorry about that.

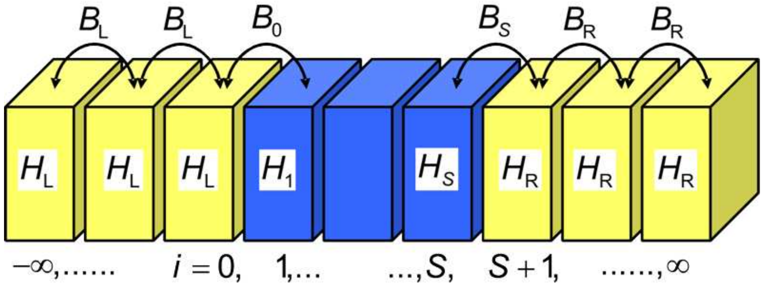

Figure 7: Hamiltonian of a tunnel junction divided into layers. The transport direction is along the horizontal. The left ($L$) and right ($R$) leads are ideal periodic wires containing the layers $i = -\infty, \ldots, 0$ and $i = S{+}1, \ldots, \infty$, respectively. The layers $i = 1, \ldots, S$ consitute the scattering region.

The wave function of Eq. 28 is generalized to

$$\boldsymbol{\psi} = \begin{pmatrix} \vdots \\ \mathbf{c}_{i-1} \\ \mathbf{c}_i \\ \mathbf{c}_{i+1} \\ \vdots \end{pmatrix}, \tag{48}$$

where $\mathbf{c}_i$ is a vector of dimension $N$. As in Sec. 1.1.2 we divide our system into three parts, with $i = -\infty, \ldots, 0$ corresponding to the left lead ($L$), $i = 1, \ldots, S$ to the scattering region ($S$) and $i = S{+}1, \ldots, \infty$ to the right lead ($R$). Within WFM the scattering problem is again solved in two steps. First the Bloch modes of the leads are calculated, then these are matched to the scattering region.

**Ideal lead modes**

The leads are assumed to be ideal wires characterized by a periodic potential. The "principal" layer is a multiple of the translational period along the wire. By construction, the Hamiltonian matrix for each layer is identical, i.e. $\mathbf{H}_i = \mathbf{H}_{L/R}$ and $\mathbf{B}_i = \mathbf{B}_{L/R}$ for the left/right leads, see Fig. 7. Eq. 32 is generalized to

$$-\mathbf{B}_{L/R}\mathbf{c}_{i-1} + (E\mathbf{1} - \mathbf{H}_{L/R})\mathbf{c}_i - \mathbf{B}^{\dagger}_{L/R}\mathbf{c}_{i+1} = 0, \tag{49}$$

with $\mathbf{1}$ the $N \times N$ identity matrix.[7] We make the same ansatz as in Eq. 34, namely that the coefficients in successive layers are connected by a Bloch factor $\lambda$

$$\mathbf{c}_{i-1} \equiv \mathbf{c} \quad ; \quad \mathbf{c}_i = \lambda\mathbf{c} \quad ; \quad \mathbf{c}_{i+1} = \lambda\mathbf{c}_i = \lambda^2\mathbf{c} \tag{50}$$

and get the equation

$$-\mathbf{B}\mathbf{c} + \lambda(E\mathbf{1} - \mathbf{H})\mathbf{c} - \lambda^2\mathbf{B}^{\dagger}\mathbf{c} = 0, \tag{51}$$

where the subscripts $L/R$ have been omitted to simplify the notation. We work at a fixed energy $E$, and Eq. 51 is a quadratic eigenvalue equation dimension $N$. The standard trick to solve such an equation is to define $\mathbf{d} = \lambda\mathbf{c}$ and convert it into

$$\left[\begin{pmatrix} \mathbf{0} & \mathbf{1} \\ -\mathbf{B} & E\mathbf{1} - \mathbf{H} \end{pmatrix} - \lambda \begin{pmatrix} \mathbf{1} & \mathbf{0} \\ \mathbf{0} & \mathbf{B}^{\dagger} \end{pmatrix}\right] \begin{pmatrix} \mathbf{c} \\ \mathbf{d} \end{pmatrix} = 0. \tag{52}$$

This is a generalized linear eigenvalue problem of dimension $2N$, which can be solved using standard numerical techniques.

---

[7] For non-orthogonal basis sets one replaces $\mathbf{1}$ by $\mathbf{S}$, the overlap matrix.

It can be shown that this equation generally has $2N$ solutions, which can be divided into $N$ right-going modes and $N$ left-going modes, labeled by "+" and "−" subscripts as in Eqs. 37 and 39. Right-going modes are either evanescent waves that are decaying to the right, or waves of constant amplitude that are propagating to the right, whereas left-going modes are decaying or propagating to the left. In contrast to the one-dimensional case, we find in three dimensions at a fixed energy in general both evanescent and propagating modes. We denote the eigenvalues and eigenvectors of Eq. 51 by

$$\lambda_{\pm,n} \quad ; \quad \mathbf{u}_{\pm,n} \quad ; \quad n = 1, \ldots, N. \tag{53}$$

Together these states form a complete basis set. In the following we assume that the vectors $\mathbf{u}_{\pm,n}$ are normalized. Note however that in general they are not orthogonal. One can easily distinguish right- from left-going evanescent modes on the basis of their eigenvalues. Right-going evanescent modes have $|\lambda_{+,n}| < 1$ and left-going evanescent modes have $|\lambda_{-,n}| > 1$, see Eq. 50. Propagating modes per definition have $|\lambda_{\pm,n}| = 1$, so here one has to determine the Bloch velocity in the propagation direction and use its sign to distinguish right from left propagation. One can show that for a tight-binding Hamiltonian, the general expression for the Bloch velocities becomes

$$v_{\pm,n} = -\frac{2a}{\hbar} \operatorname{Im}\left[\lambda_{\pm,n}\mathbf{u}_{\pm,n}^{\dagger}\mathbf{B}^{\dagger}\mathbf{u}_{\pm,n}\right], \tag{54}$$

where $a$ is the thickness of the layer [27]. In addition one can show that the Bloch velocity is non-zero only for propagating modes, i.e. evanescent states have a Bloch velocity equal to zero, as one expects on physical grounds.

Since the eigenvectors are non-orthogonal, it is convenient to define dual vectors $\widetilde{\mathbf{u}}_{\pm,n}$ by

$$\widetilde{\mathbf{u}}_{\pm,n}^{\dagger}\mathbf{u}_{\pm,m} = \delta_{n,m} \quad ; \quad \mathbf{u}_{\pm,n}^{\dagger}\widetilde{\mathbf{u}}_{\pm,m} = \delta_{n,m}. \tag{55}$$

Any wave function in the leads can be expressed as a linear combination of the lead modes. This can be done in a very compact way if we define the two $N \times N$ Bloch matrices for right- and left-going modes

$$\mathbf{F}_{\pm} = \sum_{n=1}^{N} \lambda_{\pm,n}\mathbf{u}_{\pm,n}\widetilde{\mathbf{u}}_{\pm,n}^{\dagger}. \tag{56}$$

These generalize the Bloch factors of the one-dimensional case, see Eqs. 37 and 39. One can easily construct powers of Bloch matrices

$$\mathbf{F}_{\pm}^{i} = \sum_{n=1}^{N} \lambda_{\pm,n}^{i}\mathbf{u}_{\pm,n}\widetilde{\mathbf{u}}_{\pm,n}^{\dagger}. \tag{57}$$

This expression is valid for any integer $i$, positive or negative. A general solution in the leads can now be expressed by a recursion relation

$$\mathbf{c}_i = \mathbf{c}_{+,i} + \mathbf{c}_{-,i} = \mathbf{F}_{+}^{i-j}\mathbf{c}_{+,j} + \mathbf{F}_{-}^{i-j}\mathbf{c}_{-,j}. \tag{58}$$

In a scattering problem one usually fixes the coefficients in one layer by suitable boundary conditions. Using Eq. 58 one can then determine the solution in all the layers of the leads.

### Wave function matching

The recursion relations are used to set up equations that properly match the leads to the scattering region. The scattering region is defined by the layers $i = 1, \ldots, S$, see Fig. 7. Immediately left of the scattering regions one has the recursion relation

$$\mathbf{c}_{-1} = \mathbf{F}_{L,+}^{-1}\mathbf{c}_{+,0} + \mathbf{F}_{L,-}^{-1}\mathbf{c}_{-,0}.$$

Writing $\mathbf{c}_{-,0} = \mathbf{c}_0 - \mathbf{c}_{+,0}$ one gets

$$\mathbf{c}_{-1} = \left[\mathbf{F}_{L,+}^{-1} - \mathbf{F}_{L,-}^{-1}\right]\mathbf{c}_{+,0} + \mathbf{F}_{L,-}^{-1}\mathbf{c}_0. \tag{59}$$

We introduce the scattering boundary condition as follows. The vector $\mathbf{c}_{+,0}$ is treated as the source, i.e. as the incoming wave from the left lead, e.g. a specific propagating mode of the left lead.

$$\mathbf{c}_{+,0} = \mathbf{u}_{L,+,m}. \tag{60}$$

Immediately to the right of the scattering region one has

$$\mathbf{c}_{S+2} = \mathbf{F}_{R,+}\mathbf{c}_{+,S+1} + \mathbf{F}_{R,-}\mathbf{c}_{-,S+1}.$$

We have no incoming wave from the right lead, i.e. $\mathbf{c}_{-,S+1} = 0$, so

$$\mathbf{c}_{S+2} = \mathbf{F}_{R,+}\mathbf{c}_{S+1}. \tag{61}$$

Eqs. 59 and 61 can now be used to "simplify" the tight-binding equations

$$-\mathbf{B}_i\mathbf{c}_{i-1} + (E\mathbf{1} - \mathbf{H}_i)\mathbf{c}_i - \mathbf{B}_i^\dagger\mathbf{c}_{i+1} = 0. \tag{62}$$

For $i = 0$ we write

$$\begin{aligned} &-\mathbf{B}_L\mathbf{c}_{-1} + (E\mathbf{1} - \mathbf{H}_L)\mathbf{c}_0 - \mathbf{B}_1^\dagger\mathbf{c}_1 = 0 \Leftrightarrow \\ &(E\mathbf{1} - \mathbf{H}_L - \mathbf{B}_L\mathbf{F}_{L,-}^{-1})\mathbf{c}_0 - \mathbf{B}_1^\dagger\mathbf{c}_1 = \mathbf{B}_L\left[\mathbf{F}_{L,+}^{-1} - \mathbf{F}_{L,-}^{-1}\right]\mathbf{u}_{L,+,m}. \end{aligned} \tag{63}$$

Likewise for $i = S + 1$ we write

$$\begin{aligned} &-\mathbf{B}_S\mathbf{c}_S + (E\mathbf{1} - \mathbf{H}_R)\mathbf{c}_{S+1} - \mathbf{B}_R^\dagger\mathbf{c}_{S+2} = 0 \Leftrightarrow \\ &-\mathbf{B}_S\mathbf{c}_S + (E\mathbf{1} - \mathbf{H}_R - \mathbf{B}_R^\dagger\mathbf{F}_{R,+})\mathbf{c}_{S+1} = 0. \end{aligned} \tag{64}$$

Eq. 62 with $i = 1, \ldots, S$, and Eqs. 63 and 64 are collected

$$(E\mathbf{1} - \mathbf{H}')\psi = \mathbf{Q}_{L,+,m}, \tag{65}$$

with

$$\mathbf{H}' = \begin{pmatrix} \mathbf{H}_L + \mathbf{\Sigma}_L(E) & \mathbf{B}_1^\dagger & 0 & 0 & 0 \\ \mathbf{B}_1 & \ddots & \mathbf{B}_{i-1}^\dagger & 0 & 0 \\ 0 & \mathbf{B}_{i-1} & \mathbf{H}_i & \mathbf{B}_i^\dagger & 0 \\ 0 & 0 & \mathbf{B}_i & \ddots & \mathbf{B}_S^\dagger \\ 0 & 0 & 0 & \mathbf{B}_S & \mathbf{H}_R + \mathbf{\Sigma}_R(E) \end{pmatrix}, \tag{66}$$

and

$$\boldsymbol{\psi} = \begin{pmatrix} \mathbf{c}_0 \\ \vdots \\ \mathbf{c}_i \\ \vdots \\ \mathbf{c}_{S+1} \end{pmatrix} \quad ; \quad \mathbf{Q}_{L,+,m} = \begin{pmatrix} \mathbf{B}_L\left[\mathbf{F}_{L,+}^{-1} - \mathbf{F}_{L,-}^{-1}\right]\mathbf{u}_{L,+,m} \\ \vdots \\ \mathbf{0} \\ \vdots \\ \mathbf{0} \end{pmatrix}. \tag{67}$$

As in Eq. 44 the quantities

$$\begin{aligned} \mathbf{\Sigma}_L(E) &= \mathbf{B}_L\mathbf{F}_{L,-}^{-1}; \\ \mathbf{\Sigma}_R(E) &= \mathbf{B}_R^\dagger\mathbf{F}_{R,+}, \end{aligned} \tag{68}$$

are called the "self-energies" of the left and right leads. They contain all the information about the coupling of the scattering region to the leads, as well as information on the scattering boundary conditions. The self-energies depend upon the energy $E$, since they are expressed in the Bloch matrices and thus in the lead modes and the latter have been determined at a fixed energy $E$. The self-energies are non-Hermitian, which makes the Hamiltonian $\mathbf{H}'$ non-Hermitian. Eq. 65 represents a set of linear equations of dimension $(S+2)\times N$. These can be solved using common techniques, e.g. Gaussian elimination (*LU* decomposition), followed by back substitution. Since the matrix $\mathbf{H}'$ has a block tridiagonal form (with blocks of dimension $N$), one can make use of this form to optimize the Gaussian elimination algorithm. Alternatively, since the matrices are quite sparse, one can make use of special sparse matrix techniques to solve this problem.

Transmission matrix elements are obtained by expanding the wave function in the right lead into modes

$$\mathbf{c}_{S+1} = \sum_{n-1}^{N} \mathbf{u}_{R,+,n} t'_{n,m} \;\Rightarrow\; t'_{n,m} = \widetilde{\mathbf{u}}^{\dagger}_{R,+,n}\mathbf{c}_{S+1} \tag{69}$$

and (flux) normalize them with the velocities to ensure a unitary scattering matrix,

$$t_{n,m} = \sqrt{\frac{v_{L,+,m}}{v_{R,+,n}}\frac{a_R}{a_L}}\widetilde{\mathbf{u}}^{\dagger}_{R,+,n}\mathbf{c}_{S+1} \tag{70}$$

The velocities are calculated from Eq. 54. By letting $m$ in Eqs. 60 and 67 run over all (propagating) modes $\mathbf{u}_{L,+,m}$ of the left lead, all transmission matrix elements are obtained. This sounds more complicated than it is. If one uses Gaussian elimination (*LU* decomposition) to solve Eq. 65 the elimination (decomposition) step is independent of the source vector $\mathbf{Q}_{L,+,m}$. This is the most time consuming algorithmic step. The source vector only enters in the second algorithmic step, i.e. back substitution, which is much cheaper and can easily be performed in parallel for the whole set of $\mathbf{Q}_{L,+,m}$. Moreover, if one is only interested in the transmission amplitudes, the back substitution step does not have to be fully completed, since one only needs the coefficients $\mathbf{c}_{S+1}$. If one uses sparse matrix techniques, it is possible to solve the set of linear equations in parallel for all source vectors.

Although WFM permits the calculation of amplitudes $t'_{n,m}$ of Eq. 69 between all states $n$ and $m$, i.e. propagating and evanescent, only propagating states actually contribute to the transmission. Therefore, it is possible to restrict $n$ and $m$ to propagating states only. This does not mean that one can throw out the evanescent states altogether. One needs to include them in properly matching the scattering region to the leads, cf. Eq. 68. In other words, the Bloch matrices, Eq. 57, need to be constructed from all $N$ modes, propagating and evanescent. Both of them are needed for a complete basis.

### Green function expressions

WFM can be translated into Green function expressions at the cost of loosing some of its transparency [27]. With respect to the Hamiltonian matrix of Eq. 66 a finite Green function matrix can be defined as

$$\mathbf{G}(E) = (E\mathbf{1} - \mathbf{H}')^{-1}. \tag{71}$$

It can be calculated by matrix inversion using essentially the same block Gaussian elimination scheme as used for solving the set of linear equations, Eq. 65. The matrix $\mathbf{H}'$ is non-Hermitian; its eigenvalues are not real, so the Green function matrix can be evaluated for real energies.[8]

With respect to the original infinite Hamiltonian $\mathbf{H}$ of Eq. 47 one can define the usual retarded (infinite) Green function matrix

$$\mathbf{G}^r(E) = \left[(E+i\eta)\mathbf{1} - \mathbf{H}\right]^{-1}, \tag{72}$$

where one needs the infinitesimal $\eta$ to avoid the poles on the real axis. One can show that for layers in the scattering region and $\lim_{\eta\to 0}$ one has

$$\mathbf{G}_{i,j}(E) = \mathbf{G}^r_{i,j}(E) \;\;;\;\; i,j = 0,\ldots,S+1. \tag{73}$$

---

[8] The exceptions are truly bound states of $\mathbf{H}'$. These occur at real energies, at which the Green function matrix has poles. However, these usually occur outside the energy range that is of interest for scattering. At bound state energies only evanescent modes exist in the leads, so this situation is easily identified in practice.

In terms of the Green function, the wave function in the scattering region can be written as

$$\psi = \mathbf{G}(E)\ \mathbf{Q}_{L,+,m}, \tag{74}$$

and from Eq. 69 one obtains

$$t_{n,m} = \sqrt{\frac{v_{L,+,m}}{v_{R,+,n}} \frac{a_R}{a_L}}\ \widetilde{\mathbf{u}}^{\dagger}_{R,+,n}\ \mathbf{G}_{S+1,0}(E)\ \mathbf{Q}_{L,+,m}. \tag{75}$$

After some manipulation one can obtain a Fisher-Lee expression that generalizes the one-dimensional expression of Eq. 25

$$t_{n,m} = i\hbar\sqrt{\frac{v_{R,+,n}v_{L,+,m}}{a_L a_R}}\ \widetilde{\mathbf{u}}^{\dagger}_{R,+,n}\ \mathbf{G}_{S+1,0}(E)\ \widetilde{\mathbf{u}}'_{L,+,m}. \tag{76}$$

The notation becomes a bit messy because the modes $\mathbf{u}_{L/R,+,m/n}$ are not orthogonal. If they were orthogonal, then the expression would contain $\mathbf{u}^{\dagger}_{R,+,n}\mathbf{G}_{S+1,0}(E)\mathbf{u}_{L,+,m}$. The transmission amplitude from mode $\mathbf{u}_{L,+,m}$ in the left lead to mode $\mathbf{u}_{R,+,n}$ in the right lead is determined by the Green function matrix that takes you from layer $i = 0$ to layer $i = S + 1$, i.e. across the scattering region. Proper orthogonalization of the modes leads to expressions for $\widetilde{\mathbf{u}}^{\dagger}_{R,+,n}$ and $\widetilde{\mathbf{u}}'_{L,+,m}$. The expressions can be found in Ref. [27]. The Bloch velocities $v_{L/R,+,m/n}$ make the scattering matrix unitary. Since $v_{L/R,+,m/n} \neq 0$ only for propagating states, Eq. 76 expresses explicitly that the transmission is zero whenever $n$ or $m$ describes an evanescent mode. The layer thicknesses $a_{L/R}$ are normalization factors, since our modes are normalized within a layer.

Most of the Green function expressions we obtained in the one-dimensional case can be generalized to three dimensions. The velocity of Eq. 21 becomes a velocity matrix

$$\mathbf{V}_{L/R} = -\frac{2a_{L/R}}{\hbar}\,\mathrm{Im}\,\boldsymbol{\Sigma}_{L/R}. \tag{77}$$

The matrix is diagonal and has dimension $N$ (the total number of modes). The diagonal matrix elements are the mode velocities $v_{L/R,\pm,n}$ of Eq. 54. Since $v_{L/R,\pm,n} = 0$ for evanescent states, the velocity matrices are in general singular. The transmission amplitudes of Eq. 76 can be collected in a transmission matrix $\mathbf{t}$

$$\mathbf{t} = 2i\sqrt{-\,\mathrm{Im}\,\boldsymbol{\Sigma}_R}\ \mathbf{G}_{S+1,0}(E)\ \sqrt{-\,\mathrm{Im}\,\boldsymbol{\Sigma}_L}, \tag{78}$$

which generalizes Eq. 26. The total transmission can be expressed as

$$T = \mathrm{Tr}\left[\mathbf{t}^{\dagger}\mathbf{t}\right] = 4\mathrm{Tr}\left[\mathrm{Im}\,\boldsymbol{\Sigma}_R\ \mathbf{G}^{r}_{S+1,0}(E)\ \mathrm{Im}\,\boldsymbol{\Sigma}_L\ \mathbf{G}^{a}_{0,S+1}(E)\right] \tag{79}$$

which generalizes Eq. 27 and is known as the Caroli expression or the NEGF expression [23].

# 2 Real space grid implementation: conductance of atomic wires

Application of the WFM technique for solving the scattering problem relies on a real space representation of the Kohn-Sham Hamiltonian and the wave functions. An efficient implementation based upon a high-order finite-difference scheme is discussed in Ref. [15]. In general, finite-difference schemes are suitable for treating systems with little symmetry. They have a computational efficiency that is comparable to that of plane wave basis set representations [44–47].

Similar to Eq. 2 we put the wave function $\psi$ and the Kohn-Sham one-electron potential $V$ on an equidistant grid in real space $\mathbf{r} = (x_j, y_k, z_l)$, where $x_j = x_0 + jh_x, y_k = y_0 + kh_y, z_l = z_0 + lh_z$ and $h_x, h_y, h_z$ are the grid spacings in the $x, y$ and $z$ directions, respectively. It is computationally advantageous to replace the first order finite difference approximation (FDA) of Eq. 2 by a more general, high order FDA. For the $x$ part this gives

$$\frac{\partial^2\psi(x_j, y_k, z_l)}{\partial x^2} \approx \frac{1}{h_x^2}\sum_{n=-N}^{N} c_n\psi(x_{j+n}, y_k, z_l), \tag{80}$$

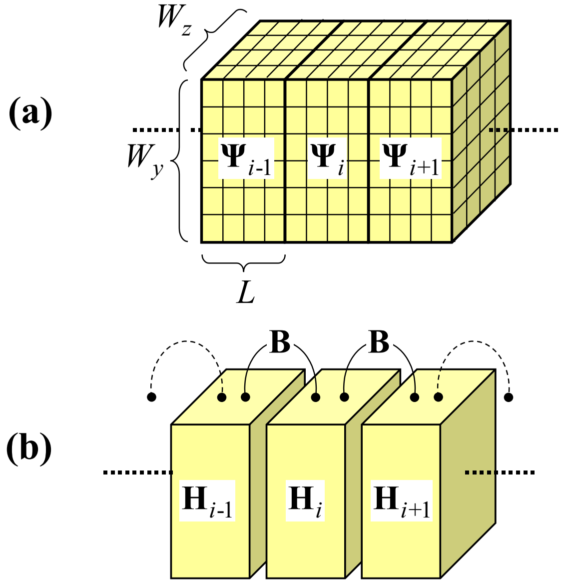

Figure 8: (a) The system is divided into cells indicated by an index $i$. The cells have $L \cdot W_y \cdot W_z$ grid points in the $x, y$ and $z$ directions, respectively. $\mathbf{\Psi}_i$ is the supervector that contains the wave function values on all grid points in cell $i$. (b) $\mathbf{H}_i$ is the Hamilton matrix connecting grid points within cell $i$; the $\mathbf{B}$-matrix connects grid points between neighboring cells and is independent of $i$.

with similar expressions for the $y$ and $z$ parts. Expressions for the coefficients $c_n$ for various values of $N$ are tabulated in Ref. [45]. The simplest approximation in Eq. (80) ($N = 1$, where $c_1 = c_{-1} = 1$ and $c_0 = -2$) reduces it to the three-dimensional equivalent of Eq. 2. However, in Ref. [15] it is demonstrated that the scattering problem can be solved much more efficiently using higher order FDA's with $N = 4$-6.

In a FDA the Kohn-Sham equation becomes

$$(E - V_{j,k,l})\,\psi_{j,k,l} + \sum_{n=-N}^{N} \left(t_n^x \psi_{j+n,k,l} + t_n^y \psi_{j,k+n,l} + t_n^z \psi_{j,k,l+n}\right) = 0, \tag{81}$$

where $V, \psi_{j,k,l}$ is a shorthand notation for $V, \psi(x_j, y_k, z_l)$ and $t_n^{x,y,z} = \hbar^2/2mh_{x,y,z}^2 \times c_n$. In order to make a connection to the formalism explained in the previous section, we divide the wire into cells of dimension $a_x \times a_y \times a_z$. The direction of the wire is given by the $x$-axis. The number of grid points in a cell is $L = a_x/h_x$ , $W_y = a_y/h_y$, $W_z = a_z/h_z$ for the $x$, $y$ and $z$ directions respectively. The values $\psi_{j,k,l}$ where the indices $j, k, l$ correspond to a single cell $i$ are grouped into a supervector $\mathbf{\Psi}_i$. The idea is shown in Fig. 8. This supervector has the dimension $N_{\text{rs}} = L \cdot W_y \cdot W_z$, which is the total number of real space grid points in a cell. If we let $i$ denote the position of the cell along the wire then Eq. (81) can then be rewritten as

$$-\mathbf{B}\mathbf{\Psi}_{i-1} + (E\mathbf{I} - \mathbf{H}_i)\mathbf{\Psi}_i - \mathbf{B}^\dagger \mathbf{\Psi}_{i+1} = 0, \tag{82}$$

for $i = -\infty, \ldots, \infty$. Here $\mathbf{I}$ is the $N_{\text{rs}} \times N_{\text{rs}}$ identity matrix. The matrix elements of the $N_{\text{rs}} \times N_{\text{rs}}$ matrices $\mathbf{H}_i$ and $\mathbf{B}$ can be derived straightforwardly from Eq. (81). The expressions are given in Ref. [15]. Clearly Eq. 82 is the same as Eq. 62, which means that we can use the WFM method to solve the scattering problem.

As a first step, the one-electron self-consistent potentials of the bulk leads and the scattering region containing the wire are obtained from DFT calculations. Subsequently the scattering problem is solved at the Fermi energy by matching the modes in the leads to the wave function in the scattering region.

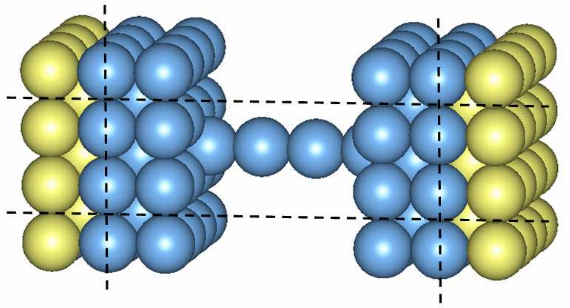

Figure 9: Structure of an atomic wire consisting of two sodium atoms between two sodium leads terminated by (001) surfaces. The boundaries of the supercell are indicated by dashed lines. Bulk atoms are indicated by yellow (light grey) balls and atoms in the scattering region by blue (dark grey) balls, respectively.

## 2.1 Conductance of monatomic sodium wires

Conductors whose cross section contains only a small number of atoms are commonly called "atomic wires". Clear evidence that the fundamental limit of a one atom cross section can be reached, has been presented for gold atomic wires [48, 49]. Over the last decade the electronic transport in atomic wires made of various metals has been characterized in great detail experimentally [50–52]. Such wires have conductances of the order of the quantum unit $G_0 = 2e^2/h$.[9] Atomic wires that have a cross section of just one atom, so-called "monatomic" wires, are the ultimate examples of quasi-one-dimensional systems. Here the effects of a reduced dimensionality are expected to be most pronounced. One of the most striking features of monatomic wires is the non-monotonic behavior of the conductance as a function of the number of atoms in the wire [53,54]. In particular, the conductance in such wires oscillates. For simple monovalent metals the oscillation has a period that corresponds to two atoms, i.e. the conductance of wires consisting of an odd number of atoms is different from that of even numbered wires. The amplitude of such oscillations is of order 0.1 $G_0$. The central questions are: what determines the phase and amplitude of the oscillation and how robust are these with respect to changes in the geometry of the wire and in the coupling between the wire and the leads?

From our first-principles calculations on sodium monatomic wires we find that odd numbered wires always have a conductance close to 1 $G_0$ and that this value is not very sensitive to changes in the geometry or in the coupling [32]. Even numbered wires have lower conductances, whose values are determined by the geometry and the coupling. This general pattern can be understood from the electronic levels of free-standing wires giving rise to transmission resonances. We analyze our first-principles results using a simple tight-binding model. In particular, we show that local charge neutrality of the sodium wires provides a strong constraint on the phase of the conductance oscillation. In absence of a significant charge transfer between the wire and the leads, a transmission resonance is pinned at the Fermi energy for wires containing an odd number of atoms, which leads to a conductance close to one quantum unit. Obtaining quantitative values for the conductance of even-numbered wires in particular, requires well-converged first-principles calculations using a realistic structure of the wire and the leads.

The one-electron potentials of the leads and the scattering regions are extracted from two self-consistent DFT calculations for bulk bcc sodium and for the supercell shown in Fig. 9, respectively, using a standard approach based upon normconserving pseudopotentials and a plane wave basis set. It turns out that, in order to obtain potentials that are converged, the total energies in such self-consistent calculations have to be converged to within $5 \times 10^{-7}$ Hartrees. One assumes that the leads outside the scattering region

---

[9] The factor of 2 with respect to Eq. 1 results from spin degeneracy.

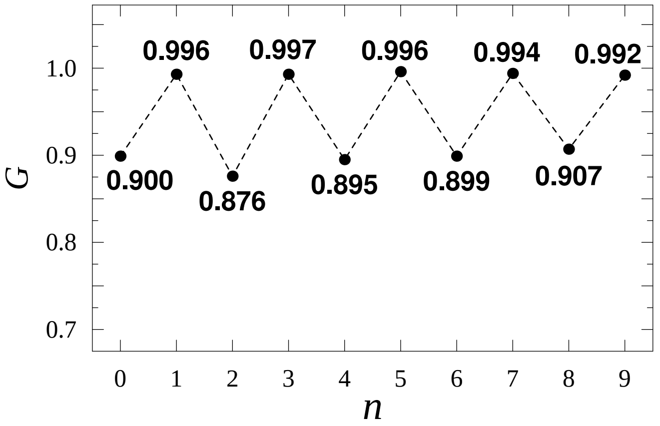

Figure 10: Conductance (in units of $G_0$) as a function of the number of atoms in the atomic chain. All atomic bond lengthes in the system are equal to the bulk value $d = 6.91a_0$.

consist of bulk material. This means that at the edges of the scattering region, the potential should join smoothly to the potentials of the bulk leads. We have checked that this is the case. Enlarging the scattering region by including two extra atomic layers in each lead changes the results reported for the conductance only by $\sim 1.5\%$ for even-numbered wires and $\lesssim 0.5\%$ for odd-numbered wires. The Fermi energy is extracted from the bulk calculation [15]. The only parameters in calculating the conductance within the finite-difference scheme are the order $N$ of the finite-difference approximation of the kinetic energy (i.e., the second derivative) and the spacing $h_{x,y,z}$ between the real-space grid points. We use $N = 4$ and $h_{x,y,z} = 0.80a_0$; for details and convergence tests we refer to Ref. [15]. The total transmission is averaged over a $8 \times 8$ $\mathbf{k}_{\|}$-point grid in the lateral BZ of the supercell. Most calculations are done for a $2 \times 2$ lateral supercell. Enlarging the supercell changes the conductance only marginally as discussed in Ref. [32].

The electron transport in the crystalline leads is ballistic, i.e. an electron goes through the leads without any scattering. The transport properties of a monatomic wire suspended between two leads depend upon three factors; the number of atoms in the chain, the geometry of the wire, and the contact between wire and leads.

The calculated conductance as a function of the number of atoms in the atomic chain is given in Fig. 10. Since a sodium atom has valence one, both the infinite sodium chain and bulk sodium have a half-filled band, and the infinite wire has one conducting channel at the Fermi level. The conductance of the infinite chain is equal to the quantum unit $G_0$, and the conductance of finite wires is $\leq G_0$. As can be observed in Fig. 10 the conductance exhibits a regular oscillation as a function of the number of atoms in the wire. The conductance is very close to $G_0$ for odd-numbered wires, and for even-numbered wires it is $\sim 10\%$ lower. Such a behavior of the conductance in atomic-sized conductors is very different from ohmic behavior in macroscopic conductors; it expresses the quantum nature of the electron transport at the nanoscale.

In order to interpret the even-odd oscillation we have calculated the conductance as a function of energy for wires of different length. The results for monatomic wires consisting of four and five atoms are shown in Fig. 11. Resonant peaks in the conductance can be clearly identified. Qualitatively they correspond to energy levels of a free-standing Na wire, which are shifted and broadened into resonances by the interaction of the wire with the leads. To illustrate this, the calculated energy levels of free-standing wires of four and five atoms are shown as bars in Fig. 11. The levels are sufficiently close to the resonant energies to warrant an interpretation of the conductance in terms of a transmission through levels of the

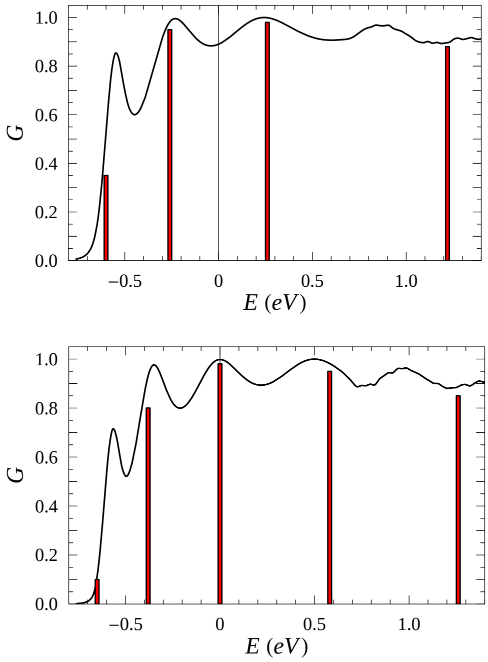

Figure 11: Conductance (in units of $G_0$) as a function of energy for monatomic wires consisting of four (top figure) and five (bottom figure) atoms. The red (grey) bars correspond to the energy levels of free-standing wires. $E = 0$ corresponds to the Fermi level.

wire. As is clearly observed in Fig. 11, the Fermi level is in between two resonant peaks for a four atom wire and right on top of a resonance for a five atom wire. By calculating the conductance as a function of energy for wires of different length it can be shown that this observation can be generalized. The Fermi level is between resonances for even-numbered wires and on top of a resonance for odd-numbered wires.

### 2.1.1 Simple tight-binding model

To support the intuitive picture presented in the previous section we use a simple tight-binding model as shown in Fig. 12, in which the leads are modeled as quasi-one-dimensional systems described by effective parameters. Here $\varepsilon_0$, $\beta$ are the on-site energies and nearest neighbor hopping coefficients of the leads, and $\varepsilon_0'$, $\beta'$ are the corresponding parameters of the wire. The coupling between the left (right) electrode and the atomic chain is given by the hopping coefficient $\beta_c$ ($\beta_c'$).

If the system has mirror symmetry, the coupling is symmetric, i.e. $\beta_c = \beta_c'$. The leads and the chain are made of the same material (sodium). If one assumes that all atoms are neutral (local charge neutrality), then it is not unreasonable to set $\varepsilon_0 = \varepsilon_0'$. The conductance can be calculated analytically for this model using WFM [27]. The parameter $\beta$ can be used as a scaling parameter. In the following all energy parameters $\varepsilon_0, \varepsilon_0', \beta', \beta_c, \beta_c'$ are in units of $\beta$. The conductance of a wire at the Fermi energy consisting of $n$ atoms is given by

$$\begin{aligned} G &= G_0, & n\,\text{odd} \\ &= G_0\,\frac{4\,\beta_c^4/\beta'^2}{\left[1+\beta_c^4/\beta'^2\right]^2}, & n\,\text{even}. \end{aligned} \tag{83}$$

The conductance for odd-numbered wires is equal to the quantum unit, and it is smaller than the quantum unit for even-numbered wires (unless by accident $\beta_c^2 = \beta'$).

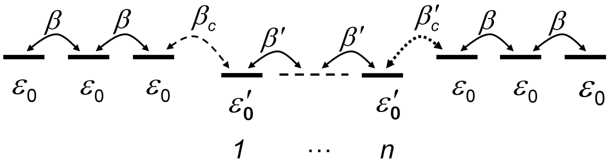

Figure 12: Tight-binding representation of the $n$-atomic wire attached to two semi-infinite one-dimensional leads.

It is instructive to study some other consequences of the tight-binding model. If $\Delta\varepsilon = \varepsilon_0 - \varepsilon_0' \neq 0$ then a charge transfer will take place between the leads and the wire. The conductance calculated at the Fermi energy for a one-site wire ($n = 1$) and a two-site wire ($n = 2$) become, respectively,

$$G = G_0 \, \frac{4\beta_c^4}{\Delta\varepsilon^2 + 4\beta_c^4}, \tag{84}$$

$$G = G_0 \, \frac{4\beta_c^4 \beta'^2}{\left[\beta_c^4 + (\beta' + \Delta\varepsilon)^2\right]\left[\beta_c^4 + (\beta' - \Delta\varepsilon)^2\right]}. \tag{85}$$

According to Eq. (84) a nonzero $\Delta\varepsilon$ suppresses the transmission through a one-site wire. The transmission is shifted “off resonance” and the conductance becomes smaller than the quantum unit. However, the coupling between wire and lead also causes a broadening of the resonance, which is proportional to $\beta_c$. This broadening partially compensates for the decrease of the conductance. If the coupling is sufficiently strong, i.e. $4\beta_c^4 \gg \Delta\varepsilon^2$, then the conductance is again close to the quantum unit. In the limit of weak coupling, i.e. $4\beta_c^4 \ll \Delta\varepsilon^2$, the conductance goes to zero with decreasing $\beta_c$ for any nonzero $\Delta\varepsilon$.

The conductance of a two-site wire, see Eq. (85), behaves qualitatively different as a function of the coupling strength $\beta_c$. In the weak coupling limit, i.e. $\beta_c^4 \ll (\beta' \pm \Delta\varepsilon)^2$ the conductance goes to zero with decreasing $\beta_c$ and the decrease is faster than for a one-site wire. Note that this only holds for $\Delta\varepsilon \ll \beta'$. If $\Delta\varepsilon \sim \beta'$ then the conductance decreases more slowly with decreasing $\beta_c$ for a two-site wire than for a one-site wire. If the coupling between wire and lead is strong, i.e. $\beta_c^4 \gg (\beta' \pm \Delta\varepsilon)^2$, then the conductance always decreases with increasing $\beta_c$. This is due to a phenomenon called “pair annihilation” of resonances [55], which happens if the resonance widths become larger than the spacing between the resonances. Between the strong and weak coupling regimes there is a value of $\beta_c$ (close to 1) where the conductance of a two-site wire is equal to the quantum unit.

The conductance of longer wires, i.e. $n > 2$, can be interpreted along the same lines. For small $\Delta\varepsilon$, the odd-numbered wires resemble the one-site wire and the even-numbered wires resemble the two-site wire. For a very large range of coupling strengths $\beta_c$ one obtains an even-odd oscillation in the conductance of a nearly constant amplitude. The conductance of odd-numbered chains is close to the quantum unit and that of even-numbered chains is smaller by an amount that depends upon the coupling between wire and lead. Apparently, this is the case that corresponds to the results of our first-principles calculations, see Fig. 10. If $\Delta\varepsilon$ becomes larger, the conductance of all wires as a function of $\beta_c$ becomes qualitatively similar to that of the two-site wire. The amplitude and even the phase of the conductance oscillation as a function of the wire length then strongly depends upon the coupling $\beta_c$ of the wire to the lead. Note that if $\Delta\varepsilon$ is significant, it will be accompanied by a significant charge transfer between wire and leads. In our first-principles calculations we have found no indication of such a large charge transfer.

In conclusion, odd-numbered wires have a conductance close to the quantum unit $G_0 = 2e^2/h$ and even-numbered wires have a lower conductance. This oscillation is remarkably robust, as we show by systematically varying the structure of the wires and the geometry of the contacts between the wires and the electrodes. The phase of the oscillation is not affected by these structural variations. The conductance of even-numbered wires is sensitive to the wire geometry. Increasing the interatomic distances in the wire and/or strengthening the contacts between wire and leads increases the conductance of even-numbered wires; increasing the asymmetry between the interatomic distances or between left and right contacts decreases the conductance.

# 3 TB-MTO implementation: layered (magnetic) structures

A computational scheme suitable for studying microscopic transport in layered magnetic materials needs to be able to describe the complex electronic structures characteristic of ($3d$) transition metal elements. In addition, it should be possible to model layered systems with different lattice parameters and to model disorder; we do this using large lateral supercells. The Local Spin-Density Approximation (LSDA) of DFT is the appropriate framework for treating itinerant electron systems from first-principles [56].

Oscillatory exchange coupling in layered magnetic structures was discussed by Bruno in terms of generalized reflection and transmission matrices [57] which were calculated by Stiles [58,59] for realistic electronic structures using a scheme [1, 2] based on linearized augmented plane waves (LAPWs). At an interface between a non-magnetic and a magnetic metal, the different electronic structures of the majority and minority spin electrons in the magnetic material give rise to strongly spin-dependent reflection [60, 61]. Schep *et al.* used transmission and reflection matrices calculated from first-principles with an embedding surface Green function method [62] to calculate spin-dependent interface resistances for specular Cu|Co interfaces embedded in diffusive bulk material [3]. The resulting good agreement with experiment indicated that interface disorder is less important than the spin-dependent reflection and transmission from a perfect interface. Calculations of domain wall resistances as a function of the domain wall thickness illustrated the usefulness of calculating the full scattering matrix [4, 63]. However, the LAPW basis set used by Stiles and Schep was computationally too expensive to allow repeated lateral supercells to be used to model interfaces between materials with very different, incommensurate lattice parameters or to model disorder. This is true of all plane-wave based basis sets which typically require of order 100 plane waves per atom in order to describe transition metal atom electronic structures reasonably well.

Muffin-tin orbitals (MTO) form a flexible, minimal basis set leading to highly efficient computational schemes for solving the Kohn-Sham equations of DFT [33,64,65]. For the close packed structures adopted by the magnetic materials Fe, Co, Ni and their alloys, a basis set of 9 functions ($s$, $p$, and $d$ orbitals) per atom in combination with the atomic sphere approximation (ASA) for the potential leads to errors in describing the electronic structure which are comparable to the absolute errors incurred by using the LSDA. The tight-binding linearized muffin tin orbital (TB-LMTO) surface Green function (SGF) method was developed to study the electronic structure of interfaces and other layered systems. When combined with the coherent-potential approximation (CPA), it allows the electronic structure, charge and spin densities of layered materials with substitutional disorder to be calculated self-consistently very efficiently [66]. MTOs thus satisfy our requirements of being able to treat complex electronic structures efficiently.

To combine the WFM method with muffin-tin orbitals, it turns out to be convenient to use the so-called "tail-cancellation" condition[10]

$$\sum_{R',l'm'} \left[ P^{\alpha}_{Rl}(\varepsilon)\delta_{RR'}\delta_{ll'}\delta_{mm'} - S^{\alpha}_{Rlm;R'l'm'} \right] c^{\alpha}_{R'l'm'} = 0, \tag{86}$$

in terms of potential functions $P^{\alpha}_{Rl}(\varepsilon)$ which characterize the AS potentials and the potential-independent

---

[10] This equation is nothing other than the KKR equation in the ASA in which the kinetic energy in the interstitial region is taken to be zero and the volume of the interstitial region is made to vanish by replacing the muffin tin spheres with space-filling atomic spheres. This choice leads to structure constants which are energy and scale independent, unlike the KKR structure constants. The potential function $P_l(\varepsilon)$ is simply related to the logarithmic derivative $D_l(\varepsilon)$ as $P_l(\varepsilon) = 2(2l+1)(D_l(\varepsilon)+l+1)/(D_l(\varepsilon)-l$.

screened structure constant matrix $S^{\alpha}_{Rlm;R'l'm'}$ whose range in real space depends on a set of screening parameters $\{\alpha_l\}$. The set of parameters which minimize the range of hopping is denoted $\alpha = \beta$. The equation analogous to Eq. (62) which we use to solve the scattering problem is then

$$-\mathbf{S}^{\beta}_{i,i-1}\mathbf{c}_{i-1} + \left(\mathbf{P}^{\beta}_{i,i}(\varepsilon) - \mathbf{S}^{\beta}_{i,i}\right)\mathbf{c}_i - \mathbf{S}^{\beta}_{i,i+1}\mathbf{c}_{i+1} = 0. \tag{87}$$

$\mathbf{c}_i$ is a $(l_{\max}+1)^2 N \equiv M$ dimensional vector consisting of the coefficients of the $i$-th layer $c_{i,Rlm}$ with $N$ atomic sites $R$ and $(l_{\max}+1)^2$ orbitals $lm$ per site.

In the actual calculation of the transmission matrix, we adopt the following procedure. First of all two separate self-consistent field calculations are performed for the left and right leads making use of their lattice periodicity to calculate the electron densities (for magnetic materials, the spin-densities) as well as corresponding Fermi energies. Next, a self consistent field calculation is carried out for the scattering region between the leads subject to the requirement that the Fermi energies in the right- and left-hand leads are equal. We now have a charge (spin) density in all space as well as the corresponding Kohn-Sham effective potential and can proceed to the solution of the transport problem.

Even though the theoretical scheme outlined above contains no adjustable parameters, its practical implementation does involve approximations, which need to be evaluated. We illustrate the formalism sketched in the previous section by calculating the transmission matrix for planar interfaces. We begin by studying ideal ordered interfaces (3.1), then describe how interface disorder can be modeled using large lateral supercells and the results analyzed using "channel decomposition" (3.2).

## 3.1 Ordered Interfaces

A recurring theme in condensed matter physics in the last twenty years has been the discovery of new physical effects and properties in systems with reduced dimensions; the prospect of exploiting these effects and properties in logical processing, sensing and storage devices is an important driving force behind nano-science and -technology. In semiconductors, the electronic structures of the electrons responsible for conduction can be described using simple models. The same is not true of the ferromagnetic transition metals which form the basis for magnetoelectronics. It is the non-trivial spin-dependence of the transmission and reflection of electrons at magnetic interfaces which provides the key to understanding phenomena such as oscillatory exchange coupling, giant- and tunneling- magnetoresistance, spin transfer torque, spin-pumping and spin injection [67]. For well-studied material combinations such as Co|Cu and Fe|Cr, modest spin-dependence of the interface transmission [3, 7, 68] of the order of 10-20% is sufficient to account for experimental observations [69].

However, the confrontation of theory and experiment just referred to is at best indirect and model-dependent. Even though the theory of transport in small structures is formulated in terms of transmission and reflection matrices [30], measuring interface transparencies directly has proven quite difficult [70]. To identify interfaces suitable for experimental study, we undertook [35] a systematic materials-specific study of the orientation dependence of the interface transmission between pairs of isostructural metals whose lattice constants match within a percent or so in the hope that it will prove possible to grow such interfaces epitaxially.

### 3.1.1 Al|Ag

One of the metal pairs we studied was Al|Ag. Both metals have the fcc crystal structure and their lattice constants are matched within 1%. Aluminium is a textbook [71] example of a system well described by the (nearly) free electron model. Silver, also usually assumed to be a free electron-like material, is a noble metal with high conductivity which is frequently used for electrical contacting. We found that in spite of the simplicity of both metals' electronic structures the transmission through Al|Ag interfaces can differ quite significantly from the predictions of the free electron model. In particular, between (111) and (001) orientations we find a factor 2 difference in interface transmission for clean Al|Ag interfaces. For free electrons the anisotropy should vanish. Our result is insensitive to interface disorder. We identify a new factor responsible for this difference which is not related to the standard velocity- [72, 73] or symmetry-mismatch [34, 39] mechanisms.

A free electron description of interface scattering, in which the effect of the crystal potential on transport is completely neglected, underlies the Blonder-Tinkham-Klapwijk or BTK theory [74] used to interpret [72, 73] Andreev reflection (AR) experiments. Point contact AR experiments are increasingly used to identify the pairing symmetry of superconductors and, in the field of magnetoelectronics, to determine the polarization of magnetic materials [75, 76]. Our finding that the electronic structure can have such a large effect on the interface transmission, implies that experiments should be analyzed using more sophisticated models.

Our study was based upon first-principles calculations of the interface electronic structure performed within the framework of density functional theory (DFT) and the local spin density approximation (LSDA). Bulk and interface potentials were determined self-consistently using the tight binding linearized muffin tin orbital (TB-LMTO) [65] surface Green's function method [66]. We assumed common lattice constants for both metals of a given structure e.g. $a_{Al} = a_{Ag} = 4.05$ Å. The potentials obtained in this way were used as input to the TB-MTO wave function-matching [7, 34] calculation of the transmission and reflection coefficients between Bloch states on either side of the interface. For disordered systems, the ASA potentials were calculated using the layer CPA (coherent potential approximation). For the scattering matrix calculation, disorder was modeled using large lateral supercells in which the CPA-ASA potentials were distributed at random in the appropriate concentrations The results of the calculations for a number of lattice-matched materials are summarized in Table 3.1.1.

The Sharvin conductances, $G_A$ and $G_B$, reported in the third and fourth columns of Table 3.1.1 are proportional to the number of states at the Fermi level propagating in the transport direction. They are properties of the bulk materials which are determined by the area of the Fermi surface projections and are a measure of the current-carrying capacity of the conductor in the ballistic regime. The largest intrinsic orientation dependence, seen to be about 13 %, is found for Mo; for Al and Ag, respectively, it is less than 8% and 5%.

The interface transmission in column five of Table 3.1.1 is expressed as a conductance, $G_{A|B} = e^2/h \sum_{\mu\nu} T_{\mu\nu}$, where $T_{\mu\nu}$ is the probability for the incoming state $\nu$ in material A to be transmitted through the interface into the outgoing state $\mu$ in material B. For most pairs of materials[11], the orientation dependence of $G_{A|B}$ is modest ($\sim$ 15% for Mo|W) and the interface conductance itself tends to be slightly smaller than the lower of the two Sharvin conductances. For these systems the behavior of the transmission appears to be determined by the projection of the Fermi surfaces. However, this is not so for Al|Ag and Al|Au interfaces. Here we observe a large anisotropy in the transport properties. The factor 2 difference in transmission between (111) and (001) orientations[12] results in a factor 4 difference between interface resistances estimated using the method of [3, 7].

The transmission probability for the (111) and (001) orientations is plotted in Figs. 13c and 13f as a function of the wave-vector component parallel to the interface, $\mathbf{k}_{\|}$, within the 2D interface Brillouin zones (BZ). A qualitative difference between the two orientations can be observed. In the (111) case, the

---

[11] Fe/Cr is an exception. For the majority spin channel, a large orientation dependence of the interface tranmission is predicted. Unlike in the case of Al/Ag, this result is very sensitive to interface disorder. In addition, a single spin channel cannot be studied directly making it difficult to obtain an unambiguous experimental result.

[12] We performed an extensive series of total energy calculations using LDA and GGA approximations to relax the various Al/Ag interfaces. Only a small dependence of the interface energy on the orientation was found. The transport calculations were repeated using the resulting relaxed geometries. The effect on the interface transmission is less than 3% which is negligible on the scale of the predicted factor of two orientation dependence.

| A\|B | | $G_A$ | $G_B$ | $G_{A\|B}$ | $2SR$ |
|---|---|---|---|---|---|
| Al\|Ag | (111) | 0.69 | 0.45 | 0.41 (0.36) | 0.64 (0.92) |
| a$_{fcc}$ = 4.05 Å | (110) | 0.68 | 0.47 | 0.30 (0.32) | 1.60 (1.39) |
| | (001) | 0.73 | 0.45 | 0.22 (0.24) | 2.82 (2.37) |
| Al\|Au | (111) | 0.69 | 0.44 | 0.41 (0.35) | 0.60 (0.99) |
| a$_{fcc}$ = 4.05 Å | (001) | 0.73 | 0.46 | 0.24 (0.26) | 2.37 (2.14) |
| Pd\|Pt | (111) | 0.62 | 0.71 | 0.55 (0.54) | 0.30 (0.33) |
| a$_{fcc}$ = 3.89 Å | (001) | 0.58 | 0.70 | 0.52 (0.51) | 0.37 (0.39) |
| W\|Mo | (001) | 0.45 | 0.59 | 0.42 (0.42) | 0.42 (0.42) |
| a$_{bcc}$ = 3.16 Å | (110) | 0.40 | 0.54 | 0.37 (0.38) | 0.52 (0.47) |
| Cu\|Co | (111)* | 0.56 | 0.47 | 0.43 (0.43) | 0.34 (0.35) |
| majority | (001) | 0.55 | 0.49 | 0.46 (0.45) | 0.26 (0.27) |
| a$_{fcc}$ = 3.61 Å | (110) | 0.59 | 0.50 | 0.46 (0.46) | 0.35 (0.35) |
| Cu\|Co | (111)* | 0.56 | 1.05 | 0.36 (0.31) | 1.38 (1.82) |
| minority | (001) | 0.55 | 1.11 | 0.32 (0.32) | 1.79 (1.79) |
| a$_{fcc}$ = 3.61 Å | (110) | 0.59 | 1.04 | 0.31 (0.35) | 1.89 (1.55) |
| Cr\|Fe | (111) | 0.61 | 0.82 | 0.27 (0.31) | 2.22 (1.84) |
| majority | (001) | 0.64 | 0.82 | 0.11 (0.25) | 7.46 (2.55) |
| a$_{bcc}$ = 2.87 Å | (110) | 0.59 | 0.78 | 0.22 (0.27) | 3.04 (2.18) |
| Cr\|Fe | (111) | 0.61 | 0.41 | 0.34 (0.34) | 0.93 (0.95) |
| minority | (001) | 0.64 | 0.46 | 0.35 (0.35) | 0.98 (0.95) |
| a$_{bcc}$ = 2.87 Å | (110)* | 0.59 | 0.40 | 0.32 (0.32) | 1.03 (1.06) |

Table 1: Sharvin conductances and interface transmissions in units of $10^{15}\Omega^{-1}m^{-2}$, interface resistances $SR$ [3,7] for ideal (and, in brackets, for disordered) interfaces in units of $10^{-15}\Omega m^2$. $S$ is the area of the sample for which R is measured. Interface disorder was modeled in 10×10 lateral supercells with two layers of 50-50 alloy. The largest uncertainty between different configurations of disorder is about 2.3%. The values given are for a single spin. For the pairs of materials and orientations indicated by a (*), comparison of the interface resistances shown in the last two columns with experimental values extracted from measurement on [3,7,34].

transmission is almost uniformly high wherever there are states on both sides of the interface. The (001) orientation exhibits more variation with high transmission in the central and outer regions of the 2D BZ but much lower in a ring-shaped region in between. The presence of this "cold ring" is the reason why the total transmission is lower for the (001) orientation. Explaining the transparency anisotropy of Al|Ag interfaces requires finding an explanation for the low transmission values in this region of the 2D BZ.

Two mechanisms are usually taken into account when analyzing the scattering at perfect interfaces. The first, velocity mismatch, is the modulation of the transmission by a factor reminiscent of the free electron formula for the transmission through a potential step: $T = 4v_Lv_R/(v_L+v_R)^2$ where $v_{L/R}$ are the components of the Fermi velocities in the transport direction on the left and right sides of the interface. This modulation is indeed present in our calculated transmissions but its effect tends to be noticeable only when one of the velocities is almost vanishingly small. Naive application of the free electron formula yields uniformly good transmission[13]independent of the orientation. Symmetry mismatch, the second

---

[13] Morover the free electron formula would lead to the violation of the unitarity of the scattering matrix (*i.e.*

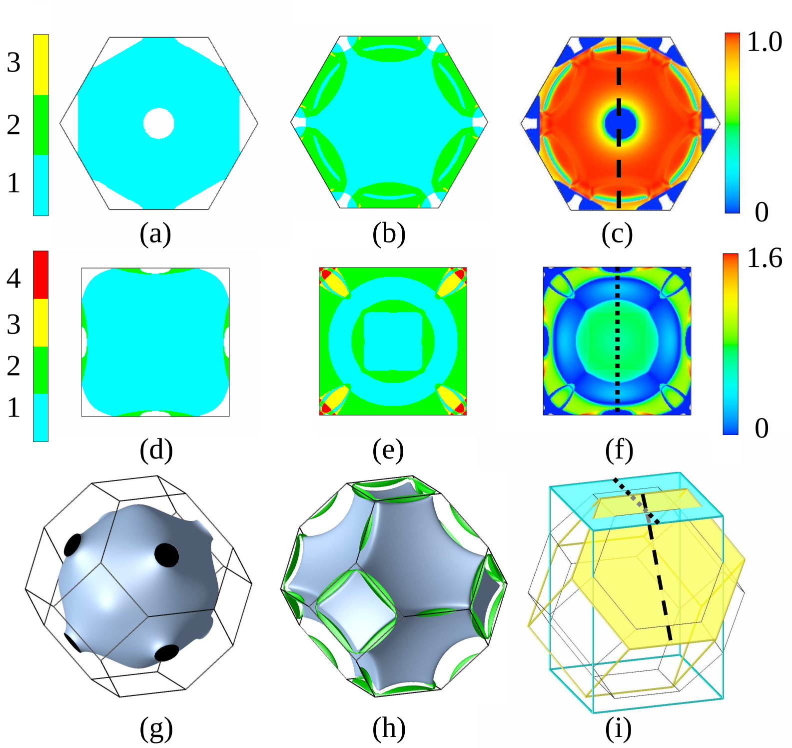

(a) (b) (c)

(d) (e) (f)

(g) (h) (i)

Figure 13: Top row: Fermi surface projections for (a) Ag, (b) Al and (c) transmission probabilities in 2DBZ for (111) orientation. Middle row: Same for (001) orientation. The color bars on the left indicate the number of scattering states in the leads for a given two dimensional wave vector $\mathbf{k}_{\|}$. The transmission probabilities indicated by the color bars on the right can exceed 1 for $\mathbf{k}_{\|}$s for which there is more than one scattering state in both Ag and Al. Bottom row: Fermi surfaces of (g) Ag and (h) Al, (i) the interface adapted BZ for (001) and (111) orientations. The vertical dashed line in (c) and on the yellow plane in panel (i) indicate the cross-section used in the left-hand panel of Fig. 14 while the vertical dotted line in (f) and on the blue plane in panel (i) indicate the cross-section used in the right-hand panel.

mechanism, can suppress the transmission between states of incompatible symmetries (*e.g.* even vs. odd etc.). Examination of the eigenvectors demonstrates that this is not the case for the Al|Ag system. For example, states on both sides of the interface, with $\mathbf{k}_{\|}$ along the vertical dotted line in Fig. 13f, are even under reflection in the plane defined by this line and the (001) transport direction. Their orbital composition $(s$,$p_y$,$p_z$,$d_{yz}$,$d_{3z^2-r^2}$,$d_{x^2-y^2}$ where the $y$ axis is parallel to the dotted line and $z$ is the transport direction) is essentially the same for both materials. The same holds for states along other symmetry lines/planes and general $\mathbf{k}_{\|}$ points (in the sense of orbital composition). The origin of the "cold ring" must be sought elsewhere.

In spite of the failure of the free electron transmission formula, this simple model serves as a useful starting point for analyzing the Fermi surface (FS) topologies. In the simplest possible approach, we model the FS of Ag (shown in Fig. 13g) as a sphere which fits into the first BZ. A larger sphere, accommodating three electrons, is needed for trivalent Al. In an extended zone scheme, conservation of momentum parallel to the interface dictates that the transmission through a specular interface is non-zero only between states with the same values of $\mathbf{k}_{\|}$; these are the $\mathbf{k}_{\|}$-vectors belonging to the region where projections of the Fermi spheres on a plane perpendicular to the transport direction overlap. For systems with lattice periodicity, we must use a downfolded FS, with fragments of the original FS sphere back-translated into

---

the conservation of particles) whenever there is more than one state on either side of the interface.

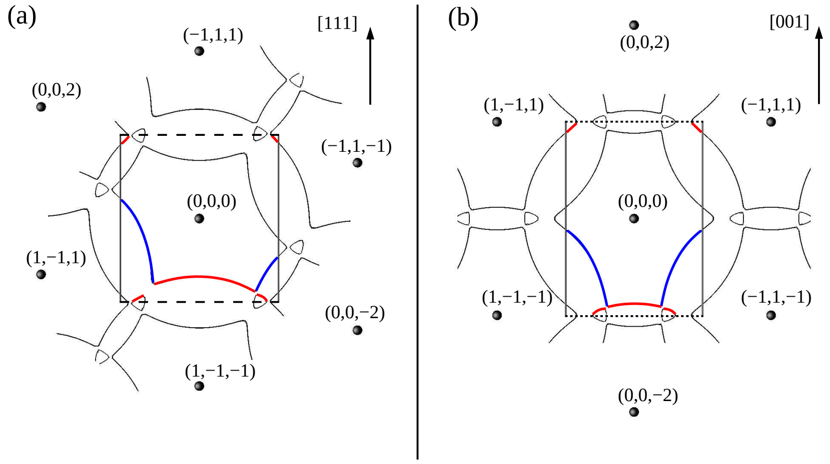

Figure 14: Intersection of a (110) plane with the Al Fermi surface and with the interface adapted BZs indicated in Fig. 13i (where the meaning of the dashed and dotted lines is explained). The labeled dots indicate the positions of the RL sites with coordinates given in units of $2\pi/a$. The red (blue) lines indicate regions of high (low) transmission.

the 1st Brillouin zone, a procedure which can be realized geometrically by placing spheres accommodating three electrons on reciprocal lattice (RL) sites and then only considering the fragments in the first BZ. Examination of the FS of Al calculated from first-principles (Fig. 13h) and its cross-section (Fig. 14) reveals that, in spite of its apparent complexity, it remains essentially (piecewise) spherical. For some values of $\mathbf{k}_{||}$ (see Figs. 13b and 13e), Al can now have more than one propagating state. Nevertheless, in the free electron limit, the downfolded states are strictly orthogonal to the states in Ag and the total transmission is unchanged. For a reduced zone scheme, we formulate the following rule: *The transmission between states in two (nearly) free electron materials which have the same* $\mathbf{k}_{||}$*, but originate from reciprocal lattice sites whose parallel components* do not *coincide, vanishes in the free electron limit and is expected to be strongly suppressed for nearly free electron like materials.*

Obviously, the truly free electron system can not exhibit anisotropy. However, in the presence of the periodic potential the original, piecewise-spherical Fermi surface and consequently the transmission is going to be modified. Firstly, since the wave functions are no longer pure plane waves, the strict orthogonality of the downfolded states is relaxed and the transmission can assume finite although typically small values (hence *suppressed* instead of *zero* in the above rule). Secondly, the shape of the Fermi surface changes with the modifications being strongest in the vicinity of RL planes where, for Al, we observe the opening of gaps between previously connected fragments. The anisotropy is mostly related to this second effect.

In Fig. 14, we show the intersection of the Al FS with a (110) plane. The two plots are rotated so that the vertical axis in Fig. 14a is the [111] direction while in Fig. 14b it is [001]. In both cases the positions of the nearest RL sites (on which spheres are centered) are shown together with the cross-section through the relevant interface-adapted Brillouin zone, which is different for each orientation; see Fig. 13i. We can now readily identify spheres from which various fragments of the Fermi surface originate and mark those fragments with positive (upward) velocities, according to the rule given above, as having high (red) or low (blue) transmissions. In the (001) case, the "high" fragments originate from (0,0,0) and (0,0,-2) centered spheres. Comparing Figs. 13f and 14b, we note that the position of the gaps opened between these spheres by Bragg reflection on the (001) and $(00\bar{1})$ planes coincides, in projection along the [001] direction, with the position of the "cold ring" in Fig. 13f. The other states present in this region originate from (1,-1,-1) (and equivalent) centered spheres, are therefore nearly orthogonal to states in Ag centered on (0,0,0) and so have low transmission. In the (111) case however, the large fragments of FS belonging to the same (1,-1,-1) sphere have high transmissions (Fig. 14a) and dominate transport. In addition, the

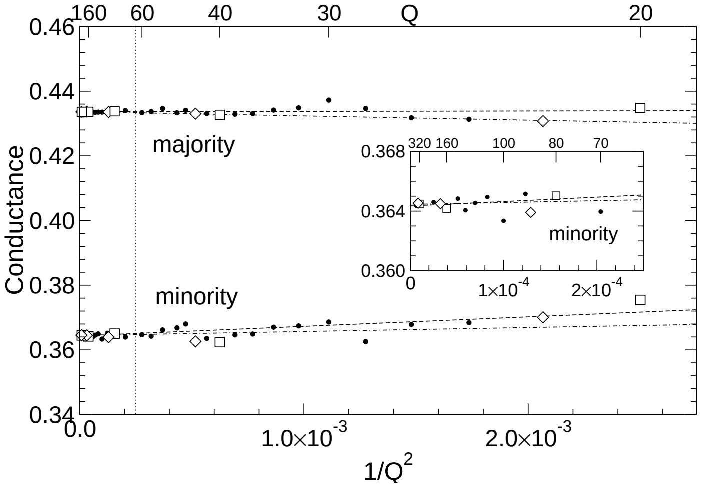

Figure 15: Interface conductance $G^{\sigma}(111)$ (in units of $10^{15}\ \Omega^{-1}\mathrm{m}^{-2}$) for an *fcc* Cu|Co(111) interface for majority and minority spins plotted as a function of the normalized area element used in the Brillouin zone summation, $\Delta^2\mathbf{k}_{\|}/A_{BZ} = 1/Q^2$. $Q$, the number of intervals along the reciprocal lattice vector is indicated at the top of the figure. The dashed line is the weighted (weighting $Q^2$) least-squares fit to the series $Q = 20, 40, 80, 160, 320$ shown as squares; the dash-dotted line is the weighted least-squares fit to the series $Q = 22, 44, 88, 176, 352$ shown as diamonds. The part of the curve for the Co minority spin case to the left of the vertical dotted line is shown on an expanded scale in the inset. An *fcc* lattice constant of $a = 3.614\mathring{A}$ and von Barth-Hedin exchange correlation potential were used.

effect of gap-opening is reduced in this orientation because of the rotation. Combination of these two factors results in the almost uniformly high transmission seen in Fig. 13c.

We can now finally identify the origin of the transmission anisotropy for Al|Ag interface. It stems from two factors: (i) the near orthogonality of the downfolded Al states to those belonging to the simple Ag sphere and (ii) the gaps opened in the continuous free electron Fermi surface by the periodic potential. The latter factor is of course related to the symmetry of the underlying crystal lattice and directly responsible for the introduction of the orientation dependence. For Al|Au interfaces, the interface transmissions and resistances are very similar to the Al|Ag case. The predicted anisotropic interface resistance and Andreev reflection (not shown) are not very sensitive to interface disorder and should be observable experimentally.

### 3.1.2 Cu|Co (111)

Our starting point is a self-consistent TB-LMTO SGF calculation [66] for the interface embedded between semi-infinite Cu and Co leads whose potentials and spin-densities were determined self-consistently in separate “bulk” calculations. The charge and spin-densities are allowed to vary in $n_{\mathrm{Cu}}$ layers of Cu and $n_{\mathrm{Co}}$ layers of Co bounding the interface. In the Cu layers, only tiny moments are induced. Only four layers away from the interface on the Co side, the magnetic moments are very close to the bulk values. At the interface, where the $d$-bandwidth is reduced as a result of the lower coordination number, the moments are suppressed rather than enhanced.

Once the interface potential has been obtained, the transmission matrix can be calculated and the BZ summation carried out. The convergence of this summation, shown in Fig. 15 for a (111) interface, a lattice constant of $a = 3.614\mathring{A}$ and an *spd* basis, closely parallels the behavior found on calculating the Sharvin conductance of the leads and does not represent a limitation in practice. Converged values of

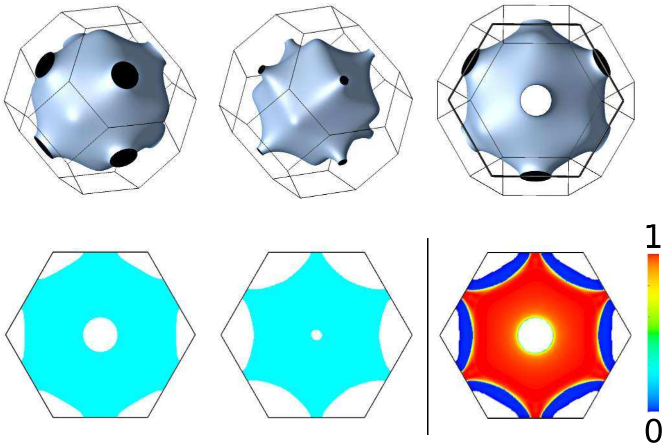

Figure 16: Top row, left-hand panel: Fermi surface (FS) of Cu; middle panel: majority-spin FS of Co; right-hand panel: Cu FS viewed along the (111) direction with a projection of the bulk fcc Brillouin zone (BZ) onto a plane perpendicular to this direction and of the two dimensional BZ. Bottom row, left-hand and middle panels: projections onto a plane perpendicular to the (111) direction of the Cu and majority-spin Co Fermi surfaces; right-hand panel: transmission probability for majority-spin states as a function of transverse crystal momentum, $T(\mathbf{k}_\parallel)$ for an *fcc* Cu|Co(111) interface.

the transmission probabilities

$$G^\sigma(\hat{n}) = \frac{e^2}{h} \sum_{m,n,\mathbf{k}_\parallel} T^\sigma_{mn}(\mathbf{k}_\parallel) = \frac{e^2}{h} \sum_{m,n,k_\parallel} |t^\sigma_{mn}(\mathbf{k}_\parallel)|^2 \tag{88}$$

are 0.434 and 0.364 in units of $10^{15}\,\Omega^{-1}\mathrm{m}^{-2}$ for majority and minority spins, respectively. The apparently modest spin-dependence of “bare” interface conductances ($\sim 20\%$) can lead to spin-dependent interface resistances differing by a factor of $\sim 3-5$. To obtain estimates of the interface resistance for highly transparent interfaces, the “bare” transmissions cannot be used. $R^{LB} = 1/G^{LB}$ results in a finite “interface” resistance, even for a fictitious interface between identical materials. Schep *et al.* [3] derived an expression for the resistance of transparent interfaces in terms of the interface transmission, which takes into account the finiteness of the conductance of the perfect leads:

$$R^{Schep}_\sigma(A|B) = \frac{h}{e^2}\left[\frac{1}{\sum T^\sigma_{mn}} - \frac{1}{2}\left(\frac{1}{N^\sigma_A} + \frac{1}{N^\sigma_B}\right)\right] \tag{89}$$

where $N^\sigma_A$ and $N^\sigma_B$ are the Sharvin conductances of the materials A and B forming the interface, in units of $e^2/h$ .

The majority-spin case can be readily understood in terms of the geometry of the Fermi surfaces of Cu and Co so we begin by discussing this simple case before examining the more complex minority-spin channel.

**Clean Cu|Co (111) Interface: Majority Spins**

In the absence of disorder, crystal momentum parallel to the interface is conserved. If, for a given value of $\mathbf{k}_\parallel$, there is a propagating state in Cu incident on the interface but none in Co, then an electron in such a state is completely reflected at the interface. Conversely, $\mathbf{k}_\parallel$’s for which there is a propagating state in Co but none in Cu also cannot contribute to the conductance. To determine the existence of such states, it is sufficient to inspect projections of the Fermi surfaces of *fcc* Cu and majority-spin Co onto a plane perpendicular to the transport direction $\hat{n}$, shown in Fig. 16 for $\hat{n} = (111)$. The first feature to note in the figure (left-hand and middle panels) is that per $\mathbf{k}_\parallel$ there is only a single channel with positive group velocity so that the transmission matrix in (88) is a complex number whose modulus squared is a transmission probability with values between 0 and 1. It is plotted in the right-hand panel and can be interpreted simply. Regions which are depicted blue correspond to $\mathbf{k}_{\|}$'s for which there are propagating states in Cu but none in Co. These states have transmission probability 0 and are totally reflected. For values of $\mathbf{k}_{\|}$ for which there are propagating states in both Cu and Co, the transmission probability is very close to one, depicted red. These states are essentially free electron-like states which have the same symmetry in both materials and see the interface effectively as a very low potential step. Close to the center of the figure there is an annular region where there are propagating states in Co but none in Cu so they do not contribute to the conductance. Performing the sum in (88), we arrive at an interface conductance of $0.43 \times 10^{15}\ \Omega^{-1}\mathrm{m}^{-2}$ to be compared to the Sharvin conductances for Cu and Co of 0.56 and 0.47 respectively, in the same units for $a = 3.614\ \mathring{A}$ and an *spd* basis. The interface conductance of 0.43 is seen to be essentially the Sharvin conductance of the majority states of Co reduced because the states closest to the $\Lambda$-axis (corresponding to the symmetry axis of the figures, the $\Gamma L$ line in reciprocal space) do not contribute.

**Clean Cu|Co (111) Interface: Minority Spins**

The minority-spin case is considerably more complex because the Co minority-spin $d$ bands are only partly filled, resulting in multiple sheets of Fermi surface. These sheets are shown in Fig. 17 together with their projections onto a plane perpendicular to the (111) transport direction. Compared to Fig. 16, one difference we immediately notice is that even single Fermi surface (FS) sheets are not single valued: for a given $\mathbf{k}_{\|}$ there can be more than one mode with positive group velocity. The areas depicted green in the projections of the FS sheets from the fourth and fifth bands are examples where this occurs.

An electron incident on the interface from the Cu side, with transverse crystal momentum $\mathbf{k}_{\|}$, is transmitted into a linear combination of all propagating states with the same $\mathbf{k}_{\|}$ in Co; the transmission matrix $t^{\sigma}_{mn}(\mathbf{k}_{\|})$ is in general not square but rectangular. The transmission probabilities $T_{mn}(\mathbf{k}_{\|})$ are shown in the bottom row of Fig. 17. Because there is only a single incident state for all $\mathbf{k}_{\|}$, the maximum transmission probability is one. Comparison of the total minority-spin transmission probability $T_{\mathcal{LR}}(\mathbf{k}_{\|})$ (Fig. 17, bottom right-hand panel) with the corresponding majority-spin quantity (right-hand panel of Fig. 16) strikingly illustrates the spin-dependence of the interface scattering, much more so than the integrated quantities might have led us to expect; the interface conductances, 0.36 and $0.43 \times 10^{15}\Omega^{-1}\mathrm{m}^{-2}$ from Table 3.1.1, differ by only $\sim 20\%$.

Three factors contribute to the large $\mathbf{k}_{\|}$-dependence of the transmission probability: first and foremost, the complexity of the Fermi surface of both materials but especially of the minority spin of Co; secondly and inextricably linked with the first because of the relationship $\hbar v_{\mathbf{k}} = \nabla_k \varepsilon(\mathbf{k})$, the mismatch of the Fermi velocities of the states on either side of the interface. Thirdly, the orbital character of the states $m$ and $n$ which varies strongly over the Fermi surface and gives rise to large matrix element effects.

The great complexity of transition metal Fermi surfaces, clear from the figure and well-documented in standard textbooks, is not amenable to simple analytical treatment and has more often than not been neglected in theoretical transport studies. Nevertheless, as illustrated particularly well by the ballistic limit [77, 78], spin-dependent band structure effects have been shown to lead to magnetoresistance ratios comparable to what are observed experimentally in the current-perpendicular-to-plane (CPP) measuring configuration and cannot be simply ignored in any quantitative discussion. Most attempts to take into account contributions of the $d$ states to electronic transport do so by mapping the five $d$ bands onto a single tight-binding or free-electron band with a large effective mass.

Fermi surface topology alone cannot explain all aspects of the transmission coefficients seen in Fig. 17. For example, there are values of $\mathbf{k}_{\|}$, such as that labeled $Y$ in the figure, for which propagating solutions exist on both sides of the interface yet the transmission probability is zero. This can be understood as follows. We begin by choosing a $(1 \times 1)$ interface unit cell so that the atoms which occupy the ABC sites

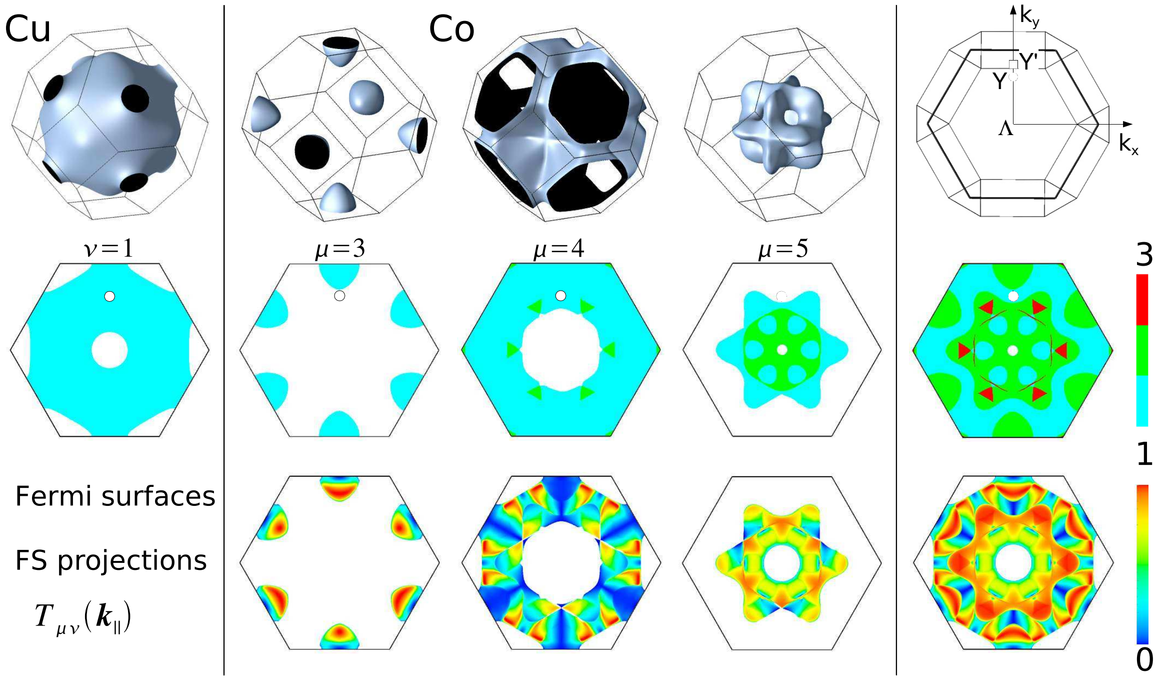

Figure 17: Top row, left-hand panel: Fermi surface (FS) of *fcc* Cu; middle panels: third, fourth and fifth FS sheets of minority-spin fcc Co; right-hand panel: projection of the bulk fcc Brillouin zone (BZ) onto a plane perpendicular to the (111) direction and of the two dimensional BZ. Middle row: corresponding projections of individual FS sheets and (rhs) of Co total. The number of propagating states with positive velocity is color-coded following the color bar on the right. Bottom row: probability $T_{\mu\nu}(\mathbf{k}_{\|})$ for a minority-spin state on the single FS sheet of Cu ($\nu = 1$) to be transmitted through a Cu|Co(111) interface into FS sheet $\mu$ of *fcc* Co as a function of the transverse crystal momentum $\mathbf{k}_{\|}$. The point Y (indicated by a small open circle) is such that there are only propagating states in Cu and in the fourth FS sheet of Co. For the point Y' (indicated by a small open square) which is slightly further away from $\Lambda$, there is, in addition, a propagating state in the third FS sheet of Co.

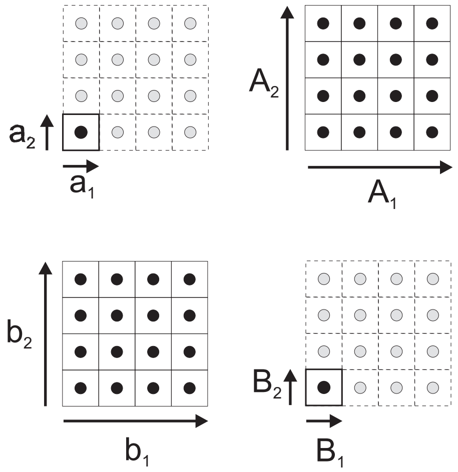

Figure 18: Illustration of lateral supercells and corresponding 2D interface Brillouin zones. Top panel: lattice vectors for a primitive unit cell containing a single atom (lhs) and a $4 \times 4$ supercell (rhs). Bottom panel: a single k-point in the BZ (rhs) corresponding to the $4 \times 4$ real-space supercell is equivalent to $4 \times 4$ k-points in the BZ (lhs) corresponding to the real-space primitive unit cell.

characteristic of the stacking in the *fcc* structure all lie along the $y$-axis. At $\mathbf{k}_{\|} = Y$, the propagating states in Cu have $\{s, p_y, p_z, d_{yz}, d_{3z^2-r^2}, d_{x^2-y^2}\}$ character and are even with respect to reflection in the plane formed by the $y$-axis and the transport direction perpendicular to the (111) plane which we choose to be the $z$-axis. For this $\mathbf{k}_{\|}$ the only propagating state in Co is in the fourth band. It has $\{p_x, d_{xy}, d_{xz}\}$ character which is odd with respect to reflection in the $yz$ plane. Consequently, the corresponding hopping matrix elements in the Hamiltonian (and in the Green function) vanish and the transmission is zero.

Along the $k_y$ axis the symmetry of the states in Cu and those in the fourth band of Co remain the same and the transmission is seen to vanish for all values of $k_y$. However, at points further away from $\Lambda$, we encounter states in the third band of Co which have even character whose matrix elements do not vanish by symmetry and we see substantial transmission probabilities. Similarly, for points closer to $\Lambda$, there are states in the fifth band of Co with even character whose matrix elements also do not vanish and again the transmission probability is substantial. Because it is obtained by superposition of transmission probabilities from Cu into the third, fourth and fifth sheets of the Co FS, the end result, though it may appear very complicated, can be straightforwardly analyzed in this manner k-point by k-point.

Though the underlying lattice symmetry is only threefold, the Fermi surface projections shown in Fig. 17 have six-fold rotational symmetry about the line $\Lambda$ because bulk $fcc$ structure has inversion symmetry (and time-reversal symmetry). The interface breaks the inversion symmetry so $T_{mn}(\mathbf{k}_{\|})$ has only threefold rotation symmetry for the individual FS sheets. However, in-plane inversion symmetry is recovered for the total transmission probability $T_{\mathcal{LR}}(-\mathbf{k}_{\|}) = T_{\mathcal{LR}}(\mathbf{k}_{\|})$ which has full sixfold symmetry.

## 3.2 Interface Disorder

Instructive though the study of perfect interfaces may be in gaining an understanding of the role electronic structure mismatch may play in determining giant magnetoresistive effects, all measurements are made on devices which contain disorder, in the diffusive regime. Because there is little information available from experiment about the nature of this disorder, it is very important to be able to model it in a flexible manner, introducing a minimum of free parameters. To model interfaces between materials with different lattice constants and disorder, we use *lateral supercells*.

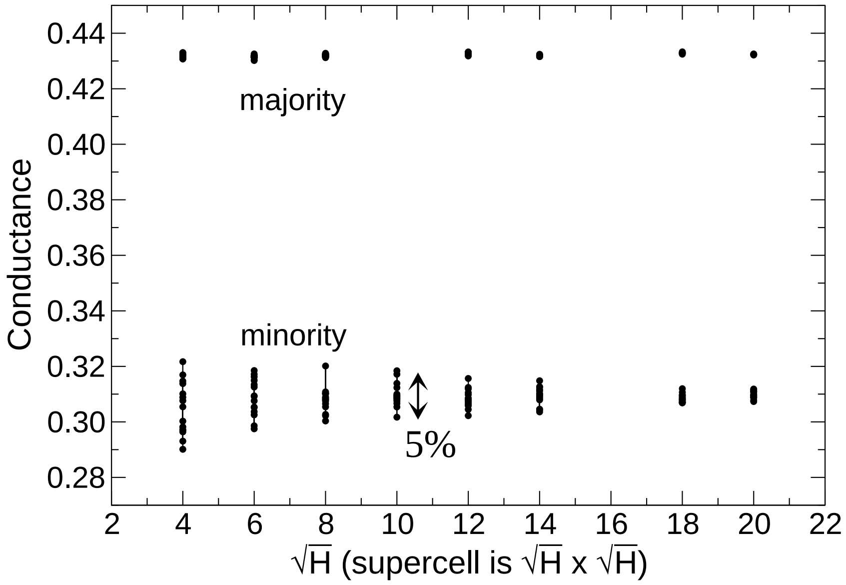

Figure 19: Interface conductance (in units of $10^{15}\Omega^{-1}\mathrm{m}^{-2}$) for a disordered Cu|Co (111) interface modeled as 2ML of 50%-50% alloy in a $\sqrt{H} \times \sqrt{H}$ lateral supercell as a function of $\sqrt{H}$. The results are given for different randomly generated configurations of disorder (15 for minority spin, 5 for majority spin). These results are for an *fcc* lattice constant of $a = 3.614\mathring{A}$, an *spd* basis and Perdew-Zunger exchange-correlation potential.

**Lateral Supercells** The TB-MTO scheme is computationally very efficient and allows us to use large lateral supercells to model in a simple fashion interface disorder, interfaces between materials whose underlying lattices are incommensurate, or quantum point contacts. This treatment becomes formally exact in the limit of infinitely large supercells. In practice, satisfactory convergence is achieved for supercells of quite moderate size.

The use of lateral supercells makes it possible to analyze diffuse scattering particularly simply. We consider an $H_1 \times H_2$ lateral supercell defined by the real-space lattice vectors

$$\mathbf{A}_1 = H_1\mathbf{a}_1 \quad \text{and} \quad \mathbf{A}_2 = H_2\mathbf{a}_2 \tag{90}$$

where $\mathbf{a}_1$ and $\mathbf{a}_2$ are the lattice vectors describing the in-plane periodicity of a primitive unit cell (Fig. 18). The cells contained within the supercell are generated by the set of translations

$$\left\{\mathbf{T}_{\parallel} = h_1\mathbf{a}_1 + h_2\mathbf{a}_2\,;\, 0 \le h_1 < H_1,\, 0 \le h_2 < H_2\right\}. \tag{91}$$

In reciprocal space the supercell Brillouin zone is defined by the reduced vectors

$$\mathbf{B}_1 = \mathbf{b}_1/H_1 \quad \text{and} \quad \mathbf{B}_2 = \mathbf{b}_2/H_2 \tag{92}$$

where $\mathbf{b}_1$ and $\mathbf{b}_2$ are the reciprocal lattice vectors corresponding to the real space primitive unit cell. As a result the Brillouin zone (BZ) is folded down, as shown schematically in Fig. 18 (bottom rhs), and the single $\mathbf{k}_{\parallel}^{\mathbb{S}}$ point ($\mathbb{S}$ is used to label supercell quantities) in the supercell BZ corresponds to the set of $H_1 \times H_2$ $\mathbf{k}$ points in the original unfolded BZ

$$\left\{\mathbf{k}_{\parallel} = h_1\mathbf{B}_1 + h_2\mathbf{B}_2\,;\, 0 \le h_1 < H_1,\, 0 \le h_2 < H_2\right\}. \tag{93}$$

Solutions associated with different $\mathbf{k}_{\parallel}$ in the primitive unit cell representation become different "bands" at the single $\mathbf{k}_{\parallel}^{\mathbb{S}}$ in the supercell representation.

The lead states are calculated using the translational symmetry of the primitive unit cell so that the computational effort scales linearly with the size of the supercell *i.e.* as $(H_1 \times H_2)$ rather than as $(H_1 \times H_2)^3$

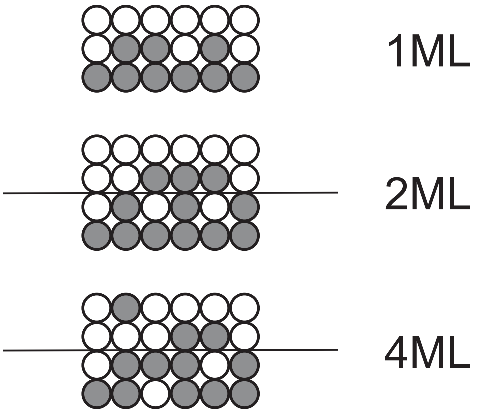

Figure 20: Illustration of 3 different models of interface disorder considered. Top (1ML): disorder is modeled using one monolayer (ML) of $[\mathrm{Cu}_{1-x}\mathrm{Co}_x]$ alloy between Cu and Co leads, denoted as $\mathrm{Cu}[\mathrm{Cu}_{1-x}\mathrm{Co}_x]\mathrm{Co}$. Middle (2ML): disorder modeled in two MLs as $\mathrm{Cu}[\mathrm{Cu}_{1-x}\mathrm{Co}_x|\mathrm{Cu}_x\mathrm{Co}_{1-x}]\mathrm{Co}$. Bottom (4ML): starting from the 2 ML disorder case, 1/3 of the concentration $x$ of impurity atoms is transferred to the next layer resulting in disorder in four MLs: $\mathrm{Cu}[\mathrm{Cu}_{1-\frac{x}{3}}\mathrm{Co}_{\frac{x}{3}}|\mathrm{Cu}_{1-\frac{2x}{3}}\mathrm{Co}_{\frac{2x}{3}}|\mathrm{Cu}_{\frac{2x}{3}}\mathrm{Co}_{1-\frac{2x}{3}}|\mathrm{Cu}_{\frac{x}{3}}\mathrm{Co}_{1-\frac{x}{3}}]\mathrm{Co}$.

which is the scaling typical for matrix operations. Another advantage is that it enables us to analyze the scattering. By keeping track of the relation between supercell "bands" and equivalent eigenmodes at different $\mathbf{k}_\parallel$ (Fig. 18) we can straightforwardly obtain $t_{mn}({\mathbf{k}_\parallel}_1, {\mathbf{k}_\parallel}_2)$ and other scattering coefficients. In other words the "interband" specular scattering in the supercell picture translates, in the presence of disorder in the scattering region, into the "diffuse" scattering between the $\mathbf{k}_\parallel$ vectors belonging to the set (93). Since this approach is formally only valid if sufficiently large supercells are used, we begin by studying how the interface conductance depends on the lateral supercell size.

To perform fully self-consistent calculations for a number of large lateral supercells and for different configurations of disorder would be prohibitively expensive. Fortunately, the coherent potential approximation (CPA) is a very efficient way of calculating charge and spin densities for a substitutional disordered $A_xB_{1-x}$ alloy with an expense comparable to that required for an ordered system with a minimal unit cell [79]. The output from such a calculation are atomic sphere potentials for the two sites, $\upsilon_A$ and $\upsilon_B$. The layer CPA approximation generalizes this to allow the concentration to vary from one layer to the next [66].

Once $\upsilon_A$ and $\upsilon_B$ have been calculated for some concentration $x$, an $N \times N$ lateral supercell is constructed in which the potentials are distributed at random, maintaining the concentration for which they were calculated self-consistently. For a given value of $N$, a number of such random distributions is generated. The conductances calculated for $4 \leq N \leq 20$ are shown in Fig. 19 for a Cu|Co(111) interface in which the Cu and the Co layers forming the interface are totally mixed to give two layers of 50%-50% interface alloy. The sample-to-sample variation is largest for the minority spin case, ranging from $\pm 5\%$ for a modest $4 \times 4$ unit cell and decreasing to about $\pm 0.5\%$ for a $20 \times 20$ unit cell. For $N \sim 10$, the spread in minority spin conductances is $\sim 3\%$ which is comparable to the typical uncertainty we associated with the LDA error, the uncertainty in lattice constants or the error incurred by using the ASA.

Comparing the conductances without and with disorder, we see that disorder has virtually no effect on the majority spin channel (0.43 versus $0.43 \times 10^{15}\,\Omega^{-1}\mathrm{m}^{-2}$) which is a consequence of the great similarity of the Cu and Co majority spin potentials and electronic structures. However, in the minority-spin channel the effect (0.36 versus $0.31 \times 10^{15}\,\Omega^{-1}\mathrm{m}^{-2}$) is much larger. Equation (89) can be used to obtain estimates

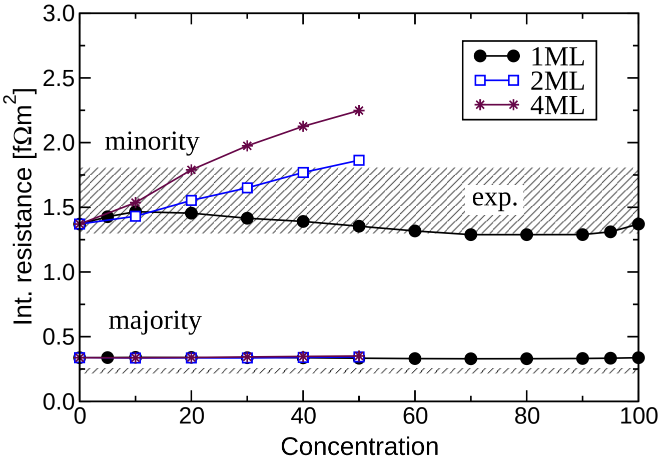

Figure 21: Interface resistance for disordered interfaces as a function of the alloy concentration used to model disordered interfaces calculated using (89). The experimental values for sputtered and MBE grown multilayers cited in Table I of Ref. [69] span a range of values which is indicated by the shaded regions.

of the interface resistances $R_\sigma^{Schep}$, which can be compared to values extracted from experiment [69, 80]. Theoretical values derived in this way for the different models of interface disorder shown in Fig. 20 are compared with experiment in Fig. 21.

The agreement of the computed interface resistances with experiments, which was already found to be good for specular interfaces of the Cu|Co systems [3, 68], is improved for minority spins by including interface disorder [7]. However, for the majority-spin case, the calculated interface resistance is *larger* than the value extracted from experiment, whether or not interface disorder is included. We will return to this again briefly after discussing how the interface scattering can be analyzed.

### 3.2.1 Analysis of Interface Disorder Scattering: Cu|Co

When disorder is modeled using lateral supercells, the transmission matrix elements can be categorized as being either *ballistic* or *diffuse*, depending upon whether or not transverse momentum is conserved. The scattering induced by two layers of 50%-50% alloy is illustrated in Figs. 22 and 23 for the majority and minority spins, respectively, of a Cu|Co(111) interface. The calculations were performed for a single $\mathbf{k}_\|$ point, $\Gamma$, and a $20 \times 20$ lateral supercell, equivalent to using a $1 \times 1$ interface cell and k-space sampling with $20 \times 20$ points in the corresponding BZ. Figs. 22(a) and 22(b) show the majority-spin Fermi surface projections of *fcc* Cu and Co, respectively, and the coarse $20 \times 20$ grid is seen to yield a good representation of the detailed Fermi surface projections shown in Fig. 16. The probability, $T(\mathbf{k}_\|, \mathbf{k}'_\|)$, that a state in Cu with transverse momentum $\mathbf{k}_\|$ is scattered on transmission through the disordered interface into the state in Co with transverse momentum $\mathbf{k}'_\|$, is shown in Fig. 22(c) for $\mathbf{k}_\| = Y$ on the $k_y$ axis (see the inset in Fig. 17) and is dominated by the $\mathbf{k}_\|$-conserving forward scattering, the *specular transmission*: $T(\mathbf{k}_\| = Y, \mathbf{k}_\| = Y) = 0.93$. Indeed, the diffuse scattering is so weak that it cannot be seen on a scale of $T$ from 0 to 1. To render it visible, a magnification by a factor 500 is needed, shown in Fig. 22(d). The total diffuse scattering, $T_{diff}(Y) = \sum_{k'_\| \neq k_\|} T(\mathbf{k}_\| = Y, \mathbf{k}_\| \neq Y) = 0.04$ can be seen from the figure to be made up of contributions of $T \sim 0.0004$ per $\mathbf{k}_\|$-point from roughly a quarter of the BZ (100 $\mathbf{k}_\|$ points) centered on $\mathbf{k}_\| = Y$. The total transmission, $T_{total} = T_{spec} + T_{diff} = 0.93 + 0.04 = 0.97$, compared to a transmission of 0.99 in the absence of disorder. In the majority case, there is thus a strong specular transmission peak surrounded by a weak diffuse background.

The minority-spin Fermi surface projections of *fcc* Cu and Co are shown in Figs. 23(a) and 23(b),

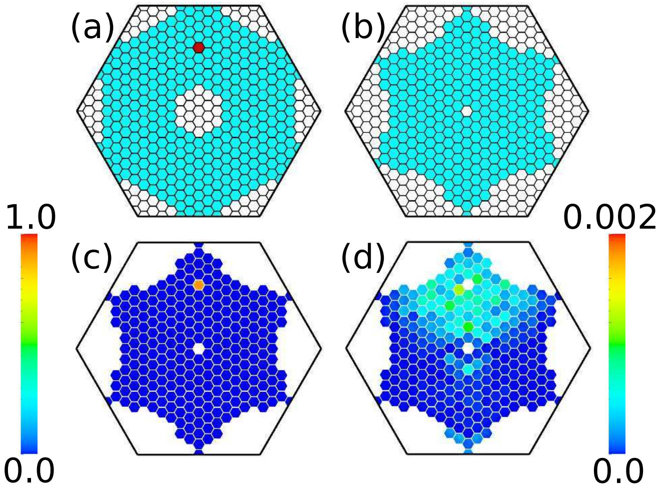

Figure 22: Fermi surface projections of majority-spin *fcc* Cu (a) and Co (b) derived from a single k-point using a $20 \times 20$ lateral supercell. The dark red point in the Cu Fermi surface projection corresponds to the point $Y$ in the top right-hand panel of Fig. 17. $T(Y, \mathbf{k}'_{\|})$ is shown in (c), and in (d) magnified by a factor 500 where the ballistic component $T(Y, \mathbf{k}'_{\|} = Y)$ is indicated by a white point because its value goes off the scale. The results were obtained by averaging over 5 different configurations of disorder.

respectively. Compared to the corresponding panels in Fig. 17, the $20 \times 20$ point representation is seen to be sufficient to resolve the individual Fermi surface sheets of Co. To study the effect of scattering, we consider two different situations. In the first, we again consider $\mathbf{k}_{\|} = Y$, for which the transmission in the absence of disorder was zero as a result of the symmetry of the states along the $k_y$ axis. $T(\mathbf{k}_{\|} = Y, \mathbf{k}_{\|})$ is shown in Fig. 23(c). By contrast with the majority-spin case just examined, there is now scattering to all other k-points in the 2D BZ, $\sum_{k'_{\|} \neq k_{\|}} T(\mathbf{k}_{\|} = Y, \mathbf{k}_{\|} \neq Y) = 0.58$. The specular transmission $T(Y, Y)$ has increased from 0.00 in the clean case, to only 0.01 in the presence of disorder. The effect of disorder is to increase the total transmission, $T_{total}(Y) = \sum_{k'_{\|}} T(\mathbf{k}_{\|} = Y, \mathbf{k}_{\|})$ from 0.00 to $T_{spec}(Y) + T_{diff}(Y) = 0.01 + 0.58 = 0.59$. Disorder thus *increases* the transmission for states which were strongly reflected in its absence.

The second case we consider is that of a k-point slightly further away from the origin $\Lambda$ along the $k_y$ axis which had a high transmission, $T(Y') = 0.98$, in the absence of disorder. For this k-point, $T(\mathbf{k}_{\|} = Y', \mathbf{k}_{\|})$, shown in Fig. 23(d), looks very similar to Fig. 23(c). There is strong diffuse scattering with $\sum_{k'_{\|} \neq k_{\|}} T(\mathbf{k}_{\|} = Y', \mathbf{k}_{\|} \neq Y') = 0.54$ while $T(Y', Y')$ has been drastically decreased from 0.98 in the clean case, to 0.06 as a result of disorder. The total transmission, $T_{total}(Y') = T_{spec}(Y') + T_{diff}(Y') = 0.06 + 0.54 = 0.60$, is almost identical to what was found for the $Y$ point. The effect of disorder has been to *decrease* the transmission of states which, in its absence, were weakly reflected. The strong k-dependence of the transmission found for the minority-spin channel in the specular case is largely destroyed by a small amount of disorder.

To derive (89), it was assumed that there is loss of coherence between adjacent interfaces. The scattering of majority-spin electrons at the Cu|Co(111) interface is so weak that this assumption is not obviously valid. It can be examined by seeing whether or not the total resistance of a Cu|Co multilayer containing N interfaces scales linearly with N. If this is so, then the incremental interface resistance $R(N) - R(N-1)$ should be independent of $N$. Note that the lead correction in (89) is independent of N and thus drops out of the incremental resistance.

The results of an extensive series of calculations for a disordered $\text{Cu}_{10}|\text{Co}_{10}(111)$ multilayer attached

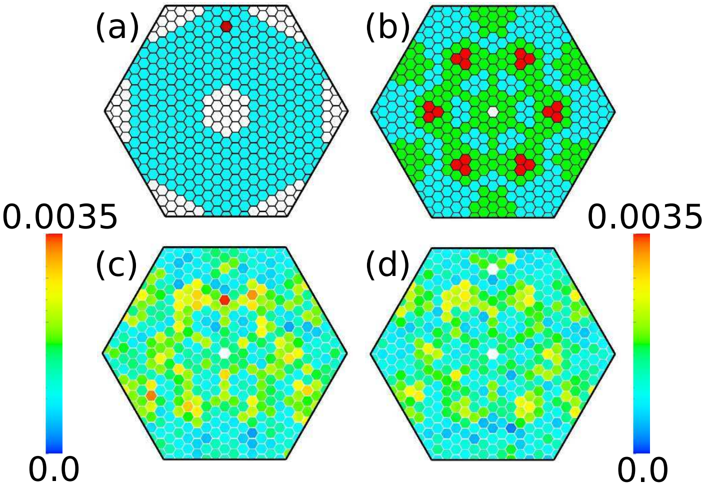

Figure 23: Fermi surface projections of minority-spin *fcc* Cu (a) and Co (b) derived from a single k-point using a 20 × 20 lateral supercell. The dark red point in the Cu Fermi surface projection corresponds to the point $Y'$ in the top right-hand panel of Fig. 17. (c) $T(Y, \mathbf{k}'_{||})$ and (d) $T(Y', \mathbf{k}'_{||})$ calculated using 20 different disorder configurations; the ballistic component $T(Y', \mathbf{k}'_{||} = Y')$ is indicated by a white point because its value goes off scale. The results were obtained by averaging over 20 different configurations of disorder.

to Cu leads are shown in Fig. 24 which includes experimental values [69] for comparison. An 10 × 10 lateral supercell was used so that, according to Fig. 19, the error on the interface transmission due to configuration averaging is negligible for the majority-spin case and of order 5% for the minority spins. In the largest calculation represented in Fig. 24, the scattering region contained about 15000 atoms: 10 × 10 lateral supercell × 150 principal layers. For the strongly scattered minority spins, the interface resistance is essentially constant for all N (within the error bar of the calculation set by the configuration averaging, choice of exchange-correlation potential etc.). For the majority spin case there is a sharp drop before the incremental resistance levels off to a constant value for $N \geq 4$ which is a factor 3 4 lower than the experimental value. This implies a breakdown of the series resistor model for the majority spins or else there is some other source of majority-spin scattering which has not been included in the calculation. Including bulk scattering does not change this result significantly. Other materials specific studies of the transport properties of Cu|Co multilayers carried out with other methods [81] also find that substitutional disorder alone cannot account for the reported resistivities in the majority-spin channel.

### 3.2.2 Cr|Fe (100)

An extreme example of how interface disorder can *enhance* interface transmission is found for the bcc(100) orientation of Cr|Fe. Whereas the majority-spin band structures were well matched in the case of Cu|Co, the situation is reversed for Cr|Fe and it is the minority-spin electronic structures which match well. Calculating the interface resistance $SR$ using (89), we find values of 3.73 f$\Omega$m$^2$ and 0.49 f$\Omega$m$^2$ for majority and minority spin, respectively, in the absence of disorder and values of 1.27 f$\Omega$m$^2$ and 0.47 f$\Omega$m$^2$, respectively when interface disorder is modeled as two layers of 50-50 alloy as was done for Cu|Co. Thus disorder reduces the majority-spin interface resistance by almost a factor of three while having only a small effect on the well-matched minority spin channel, just as in the Cu|Co majority spin case.

The qualitative difference between Cr|Fe and Cu|Co can be understood in terms of their Fermi surface

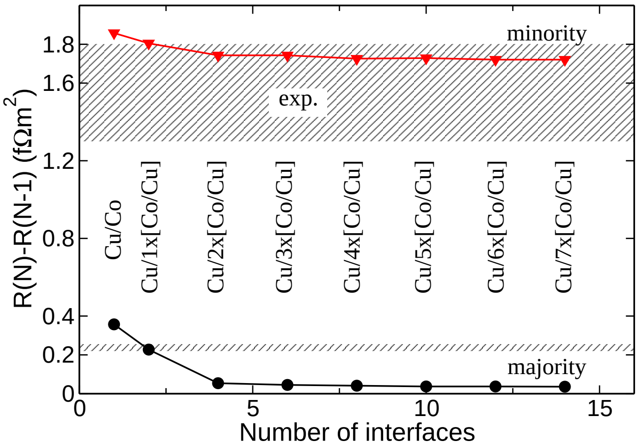

Figure 24: Differential interface resistance as the number of interfaces increase for a disordered Cu|Co(111) multilayer embedded between Cu leads. A 10 × 10 lateral supercell was used and the interface was modeled as two layers of 50%-50% alloy (2ML model). The results represent an average over 5 disorder configurations. The range of experimental values [69] is indicated by the shaded regions.

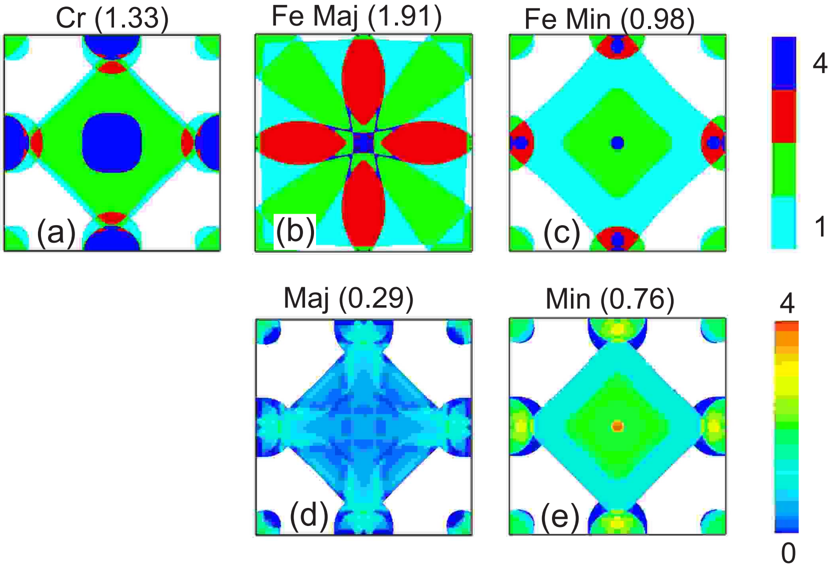

Figure 25: Fermi surface projections of *bcc* (a) non-magnetic Cr, (b) Fe, majority-spin and (c) Fe, minority-spin. (d) and (e) show the majority- respectively, minority-spin interface transmissions for a clean lattice-matched *bcc* Cr|Fe interface. The result of integrating the number of channels over the whole Brillouin zone is given in brackets at the top of each panel.

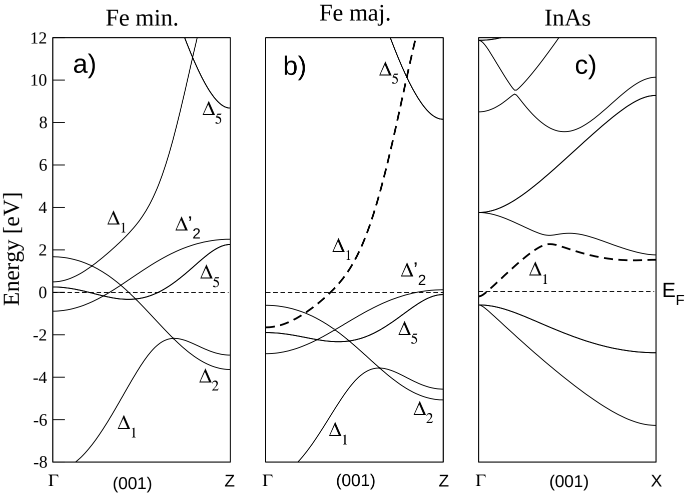

Figure 26: Energy band structures of tetragonal Fe minority spin states (a), majority spin states (b), and InAs states (c) at $\mathbf{k}_{\parallel} = 0$ for $\mathbf{k} = (00k_z)$ perpendicular to the interface.

projections and transmission probabilities $T_{\mathcal{LR}}(\mathbf{k}_{\parallel})$. In the Cu|Co(111) majority-spin case (Fig. 16), there was a large area of the 2D BZ where states on both sides matched very well and interface disorder led to mainly forward scattering with virtually no reduction of the total transmission. In the minority-spin case (Fig. 17), the situation was more complicated because the average transmission was much lower in the absence of disorder (∼ 60%) and the disorder-induced reduction of the interface transmission (∼ 20%) resulted from two competing effects: transmission enhancement by symmetry-breaking for channels which were closed for reasons of symmetry and transmission reduction by diffuse scattering for channels which were very transparent in the absence of disorder. On balance, defect scattering reduced the transmission probability and thus *increased* the interface resistance of the Cu|Co minority spin channel.

In spite of there being multiple sheets of Cr and majority-spin Fe Fermi surfaces which overlap in large regions of the 2D Brillouin zone (see Figs. 25(a-c)), the average majority-spin transmission probabilities in the absence of disorder, shown in Fig. 25(d), are very small throughout the BZ while those for the minority-spin case, shown in Fig. 25(e), are quite substantial. As in the Cu|Co case, there are two mechanisms by which interface disorder *increases* the interface transmission. Majority-spin electrons with small $\mathbf{k}_{\parallel}$ are almost completely reflected at the clean Cr|Fe interface because the electronic states on both sides of the interface do not match well. Defect scattering is found to increase the transmission of these electrons strongly. Furthermore, for large areas of the two-dimensional Brillouin zone, there are no propagating states on the Cr side. Propagating modes in Fe with these values of $\mathbf{k}_{\parallel}$, which were inaccessible to Cr electrons in the ordered case, can be reached by diffusive scattering. This opens up a large number of new channels and this increase in transmission for the Cr|Fe majority-spin channel translates into a reduction by a factor 3 of the interface resistance. Recent CPP experiments on Fe|Cr(110) [82] show that the spin-averaged resistance agrees very well with the theoretical prediction, but not the polarization dependence.

### 3.2.3 Spin-injection, spin-tunneling

Spin-dependent matching of electronic structures not only plays a role at interfaces between metallic ferromagnets and non-magnetic metals. It also occurs at the interface between itinerant ferromagnets and semiconductors or insulators[14] where the electronic structure of the semiconductor/insulator in a very

---

[14] The term "Spintronics" is used to refer to the study of spin-dependent transport in semiconductors while "Magnetoelectronics" is used to refer either to spin-dependent transport in metallic systems or to spin-dependent

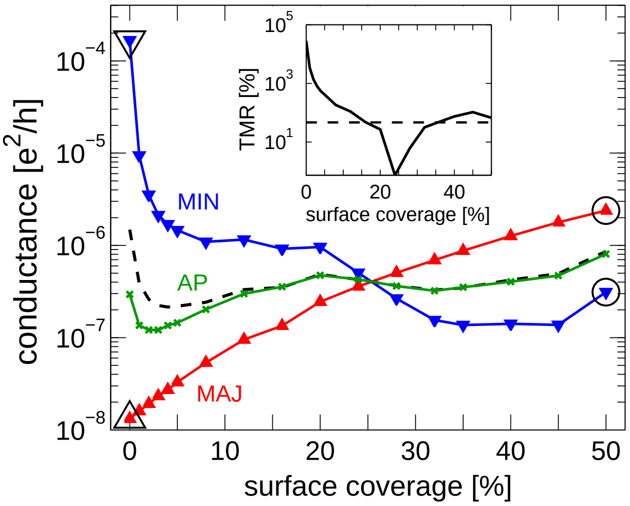

Figure 27: Configuration-averaged conductances $G_P^{min}$ (▼), $G_P^{maj}$ (▲), and $G_{AP}^{\sigma}$ (×) of an Fe|vacuum|Fe magnetic tunnel junction with 8 ML thick vacuum barrier as a function of the surface coverage, normalized to a 1 × 1 surface unit cell. The dashed line denotes $G_{AP}^{\sigma} = \sqrt{G_P^{maj} G_P^{min}}$. Inset: TMR as a function of the surface coverage. The dashed line is the value predicted using Julliere's expression and a calculated DOS polarization of 55%.

small region of reciprocal space dominates the injection/tunneling as in Fig. 26. This happens when there is lattice matching and in the absence of disorder so transverse crystal momentum is conserved. Most work has focussed on systems containing Fe(001)-related interfaces because in this orientation the lattice constant of Fe is reasonably well matched to those of a number of inorganic semiconductors and to MgO. The electronic structures were either calculated directly from first-principles [20, 39, 83–91] or obtained by fitting to first-principles electronic structures [16, 18, 21, 22, 92]. For disorder-free interfaces, very large polarizabilities of the injection or tunnel currents are predicted, much larger than those measured so far, including the recent experiments on single-crystal MgO-based tunnel junctions [93–95].

Unlike metallic systems, the current in semiconductors or tunnel junctions is carried by a very small number of channels. A realistic description of transport in such systems requires describing these channels accurately. Calculations in which interface roughness and/or disorder were considered [39, 42] show that injection polarization depends sensitively on the detailed interface structure. Even a small amount of roughness (Fig. 27) or disorder (Fig. 28) is sufficient to quench the huge theoretical values of tunneling magnetoresistance predicted for ideal magnetic tunnel junctions to values comparable to those observed in experiment. While the quality of tunnel junctions is clearly improving, much more work needs to be done to characterize the experimental disorder quantitatively.

## 3.3 Outlook

So far we have been concerned with the quantitative and qualitative characteristics of the transmission and reflection of electron states at *single* interfaces between real materials, one of which is an itinerant ferromagnet. The advantage of focussing on the full scattering matrix, rather than simply calculating the conductance, is that it provides us with greater insight and is a very convenient point of contact with other theories, such as random matrix theory [30] or circuit theory [31]. By interfacing with phenomenological theories, we can make contact relatively easily with more complex transport problems. A

---

transport in general, including both Spintronics, giant magnetoresistance (GMR) and tunneling magnetoresistance (TMR).

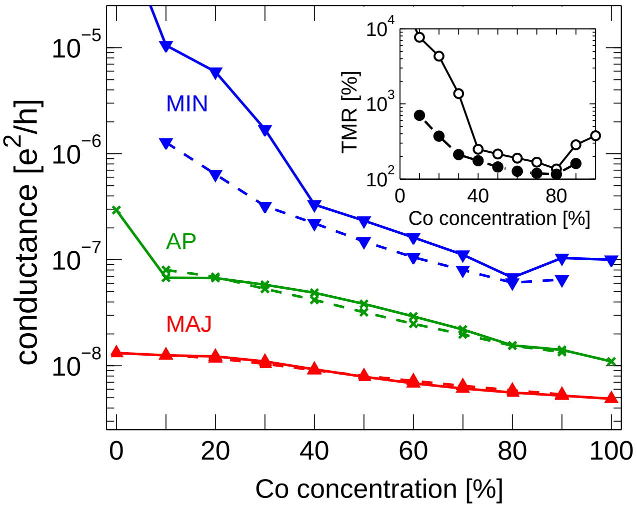

Figure 28: $G_P^{min}$ (▼), $G_P^{maj}$ (▲), and $G_{AP}^{\sigma}$ (×) for an Fe$_{1-x}$Co$_x$|vacuum|Fe$_{1-x}$Co$_x$ magnetic tunnel junction with 8 ML thick vacuum barrier as a function of $x$, the concentration of Co atoms, calculated in the virtual crystal (VCA: solid lines) and CPA/supercell (SC: dashed lines) approximations. Conductances are configuration averaged and normalized to a $1 \times 1$ surface unit cell. Inset: TMR in VCA (○) and CPA/SC (●) approximations.

good example of this is the study of the materials dependence of the suppression of Andreev scattering at a ferromagnetic|superconducting interface. This is a problem which had been studied phenomenologically [30] without taking into account details of the electronic structure of materials which might be used in an actual experiment. Because it had been formulated in terms of the scattering matrix for the F|S interface with the superconducting material in its normal state, it was straightforward to introduce and study the dependence on the constituent materials [38]. We argue that such an approach may be more fruitful than a frontal, brute force approach to calculating transport properties entirely from first principles.

## References

[1] M. D. Stiles and D. R. Hamann, Phys. Rev. B **38**, 2021 (1988).

[2] M. D. Stiles and D. R. Hamann, Phys. Rev. Lett. **66**, 3179 (1991).

[3] K. M. Schep, J. B. A. N. van Hoof, P. J. Kelly, G. E. W. Bauer, and J. E. Inglesfield, Phys. Rev. B **56**, 10805 (1997).

[4] J. B. A. N. van Hoof, K. M. Schep, A. Brataas, G. E. W. Bauer, and P. J. Kelly, Phys. Rev. B **59**, 138 (1999).

[5] J. M. MacLaren, X.-G. Zhang, W. H. Butler, and X. Wang, Phys. Rev. B **59**, 5470 (1999).

[6] J. Kudrnovský, V. Drchal, C. Blaas, P. Weinberger, I. Turek, and P. Bruno, Phys. Rev. B **62**, 15084 (2000).

[7] K. Xia, P. J. Kelly, G. E. W. Bauer, I. Turek, J. Kudrnovský, and V. Drchal, Phys. Rev. B **63**, 064407 (2001).

[8] I. Riedel, P. Zahn, and I. Mertig, Phys. Rev. B **63**, 195403 (2001).

[9] J. Taylor, H. Guo, and J. Wang, Phys. Rev. B **63**, 245407 (2001).

[10] M. Brandbyge, J. L. Mozos, P. Ordejón, J. Taylor, and K. Stokbro, Phys. Rev. B **65**, 165401 (2002).

[11] D. Wortmann, H. Ishida, and S. Blügel, Phys. Rev. B **65**, 165103 (2002).

[12] D. Wortmann, H. Ishida, and S. Blügel, Phys. Rev. B **66**, 075113 (2002).

[13] K. S. Thygesen, M. V. Bollinger, and K. W. Jacobsen, Phys. Rev. B **67**, 115404 (2003).

[14] P. Mavropoulos, N. Papanikolaou, and P. Dederichs, Phys. Rev. B **69**, 125104 (2004).

[15] P. A. Khomyakov and G. Brocks, Phys. Rev. B **70**, 195402 (2004).

[16] E. Y. Tsymbal and D. G. Pettifor, J. Phys.: Condens. Matter. **9**, L411 (1997).

[17] J. Mathon, Phys. Rev. B **55**, 960 (1997).

[18] J. Mathon, Phys. Rev. B **56**, 11810 (1997).

[19] S. Sanvito, C. J. Lambert, J. H. Jefferson, and A. M. Bratkovsky, Phys. Rev. B **59**, 11936 (1999).

[20] W. H. Butler, X. G. Zhang, T. C. Schulthess, and J. M. MacLaren, Phys. Rev. B **63**, 054416 (2001).

[21] J. Mathon and A. Umerski, Phys. Rev. B **63**, 220403 (2001).

[22] J. Mathon and A. Umerski, Phys. Rev. B **71**, 220402 (2005).

[23] C. Caroli, R. Combescot, P. Nozières, and D. Saint-James, J. Phys. C: Sol. State Phys. **4**, 916 (1971).

[24] D. S. Fisher and P. A. Lee, Phys. Rev. B **23**, 6851 (1981).

[25] T. Ando, Phys. Rev. B **44**, 8017 (1991).

[26] P. S. Krstić, X.-G. Zhang, and W. H. Butler, Phys. Rev. B **66**, 205319 (2002).

[27] P. A. Khomyakov, G. Brocks, V. Karpan, M. Zwierzycki, and P. J. Kelly, Phys. Rev. B **72**, 035450 (2005).

[28] J. E. Inglesfield, J. Phys. C: Sol. State Phys. **14**, 3795 (1981).

[29] S. Crampin, J. B. A. N. van Hoof, M. Nekovee, and J. E. Inglesfield, J. Phys.: Condens. Matter. **4**, 1475 (1992).

[30] C. W. J. Beenakker, Rev. Mod. Phys. **69**, 731 (1997).

[31] A. Brataas, G. E. W. Bauer, and P. J. Kelly, Phys. Rep. **427**, 157 (2006).

[32] P. A. Khomyakov and G. Brocks, Phys. Rev. B **74**, 165416 (2006).

[33] O. K. Andersen, Z. Pawlowska, and O. Jepsen, Phys. Rev. B **34**, 5253 (1986).

[34] K. Xia, M. Zwierzycki, M. Talanana, P. J. Kelly, and G. E. W. Bauer, Phys. Rev. B **73**, 064420 (2006).

[35] P. X. Xu, K. Xia, M. Zwierzycki, M. Talanana, and P. J. Kelly, Phys. Rev. Lett. **96**, 176602 (2006).

[36] K. Xia, P. J. Kelly, G. E. W. Bauer, A. Brataas, and I. Turek, Phys. Rev. B **65**, 220401 (2002).

[37] M. Zwierzycki, Y. Tserkovnyak, P. J. Kelly, A. Brataas, and G. E. W. Bauer, Phys. Rev. B **71**, 064420 (2005).

[38] K. Xia, P. J. Kelly, G. E. W. Bauer, and I. Turek, Phys. Rev. Lett. **89**, 166603 (2002).

[39] M. Zwierzycki, K. Xia, P. J. Kelly, G. E. W. Bauer, and I. Turek, Phys. Rev. B **67**, 092401 (2003).

[40] G. E. W. Bauer, A. Brataas, Y. Tserkovnyak, B. I. Halperin, M. Zwierzycki, and P. J. Kelly, Phys. Rev. Lett. **92**, 126601 (2004).

[41] G. E. W. Bauer, Y. Tserkovnyak, A. Brataas, J. Ren, K. Xia, M. Zwierzycki, and P. J. Kelly, Phys. Rev. B **72**, 155304 (2005).

[42] P. X. Xu, V. M. Karpan, K. Xia, M. Zwierzycki, I. Marushchenko, and P. J. Kelly, Phys. Rev. B **73**, 180402 (2006).

[43] S. Datta, *Electronic Transport in Mesoscopic Systems* (Cambridge University Press, Cambridge, 1995).

[44] J. R. Chelikowsky, N. Troullier, and Y. Saad, Phys. Rev. Lett. **72**, 1240 (1994).

[45] J. R. Chelikowsky, N. Troullier, K. Wu, and Y. Saad, Phys. Rev. B **50**, 11355 (1994).

[46] T. Ono and K. Hirose, Phys. Rev. B **82**, 5016 (1999).

[47] Y. Fujimoto and K. Hirose, Phys. Rev. B **67**, 195315 (2003).

[48] A. I. Yanson, G. Rubio-Bollinger, H. E. van den Brom, N. Agraït, and J. M. Ruitenbeek, Nature **395**, 783 (1998).

[49] H. Ohnishi, Y. Kondo, and K. Takayanagi, Nature **395**, 780 (1998).

[50] N. Agraït, A. L. Yeyati, and J. M. van Ruitenbeek, Phys. Rep. **377**, 81 (2003).

[51] J. M. Krans, J. M. van Ruitenbeek, V. V. Fisun, I. K. Yanson, and L. J. Jongh, Nature **375**, 767 (1995).

[52] A. Yazdani, D. M. Eigler, and N. D. Lang, Science **272**, 1921 (1996).

[53] F. Yamaguchi, T. Yamada, and Y. Yamamoto, Sol. State Comm. **102**, 779 (1997).

[54] N. D. Lang, Phys. Rev. Lett. **79**, 1357 (1997).

[55] H.-W. Lee and C. S. Kim, Phys. Rev. B **63**, 075306 (2001).

[56] J. Kübler, *Theory of Itinerant Electron Magnetism* (Oxford University Press, Oxford, 2002).

[57] P. Bruno, J. Magn. & Magn. Mater. **121**, 248 (1993).

[58] M. D. Stiles, Phys. Rev. B **48**, 7238 (1993).

[59] M. D. Stiles, J. Appl. Phys. **79**, 5805 (1996).

[60] S. F. Zhang and P. M. Levy, J. Appl. Phys. **69**, 4786 (1991).

[61] S. F. Lee, W. Pratt Jr., Q. Yang, P. Holody, R. Loloee, P. A. Schroeder, and J. Bass, J. Magn. & Magn. Mater. **118**, L1 (1993).

[62] J. B. A. N. van Hoof, *The Embedding Method*, PhD thesis, University of Nijmegen, Nijmegen, The Netherlands, 1997.

[63] J. B. A. N. van Hoof, K. M. Schep, P. J. Kelly, and G. E. W. Bauer, J. Magn. & Magn. Mater. **177-181**, 188 (1998).

[64] O. K. Andersen and O. Jepsen, Phys. Rev. Lett. **53**, 2571 (1984).

[65] O. K. Andersen, O. Jepsen, and D. Glötzel, Canonical description of the band structures of metals in, in *Highlights of Condensed Matter Theory*, edited by F. Bassani, F. Fumi, and M. P. Tosi, International School of Physics 'Enrico Fermi', Varenna, Italy,, pp. 59–176, North-Holland, Amsterdam, 1985.

[66] I. Turek, V. Drchal, J. Kudrnovský, M. Šob, and P. Weinberger, *Electronic Structure of Disordered Alloys, Surfaces and Interfaces* (Kluwer, Boston-London-Dordrecht, 1997).

[67] see the collection of articles, in *Ultrathin Magnetic Structures I-IV*, edited by J. A. C. Bland and B. Heinrich, Springer-Verlag, Berlin, 1994-2005.

[68] M. D. Stiles and D. R. Penn, Phys. Rev. B **61**, 3200 (2000).

[69] J. Bass and W. P. Pratt Jr., J. Magn. & Magn. Mater. **200**, 274 (1999).

[70] C. Galinon, K. Tewolde, R. Loloee, W. C. Chiang, S. Olson, H. Kurt, W. P. Pratt Jr., J. Bass, P. X. Xu, K. Xia, and M. Talanana, Appl. Phys. Lett. **86**, 182502 (2005).

[71] N. W. Ashcroft and N. D. Mermin, *Solid State Physics* (Holt-Saunders International Editions, Philadelphia, 1976).

[72] I. I. Mazin, Phys. Rev. Lett. **83**, 1427 (1999).

[73] I. I. Mazin, A. A. Golubov, and B. Nadgorny, J. Appl. Phys. **89**, 7576 (2001).

[74] G. E. Blonder, M. Tinkham, and T. M. Klapwijk, Phys. Rev. B **25**, 4515 (1982).

[75] R. J. Soulen Jr., J. M. Byers, M. S. Osofsky, B. Nadgorny, T. Ambrose, S. F. Cheng, P. R. Broussard, C. T. Tanaka, J. Nowak, J. S. Moodera, A. Barry, and J. M. D. Coey, Science **282**, 85 (1998).

[76] S. K. Upadhyay, A. Palanisami, R. N. Louie, and R. A. Buhrman, Phys. Rev. Lett. **81**, 3247 (1998).

[77] K. M. Schep, P. J. Kelly, and G. E. W. Bauer, Phys. Rev. Lett. **74**, 586 (1995).

[78] K. M. Schep, P. J. Kelly, and G. E. W. Bauer, Phys. Rev. B **57**, 8907 (1998).

[79] P. Soven, Phys. Rev. **156**, 809 (1967).

[80] W. P. Pratt, Jr., S. F. Lee, J. M. Slaughter, R. Loloee, P. A. Schroeder, and J. Bass, Phys. Rev. Lett. **66**, 3060 (1991).

[81] P. Zahn, J. Binder, and I. Mertig, Phys. Rev. B **68**, 100403 (2003).

[82] A. Zambano, K. Eid, R. Loloee, W. P. Pratt, Jr., and J. Bass, J. Magn. & Magn. Mater. **253**, 51 (2002).

[83] J. M. MacLaren, X.-G. Zhang, and W. H. Butler, Phys. Rev. B **56**, 11827 (1997).

[84] J. M. MacLaren, W. H. Butler, and X.-G. Zhang, J. Appl. Phys. **83**, 6521 (1998).

[85] H. C. Herper, P. Weinberger, A. Vernes, L. Szunyogh, and C. Sommers, Phys. Rev. B **64**, 184442 (2001).

[86] O. Wunnicke, P. Mavropoulos, R. Zeller, P. H. Dederichs, and D. Grundler, Phys. Rev. B **65**, 241306 (2002).

[87] P. Mavropoulos, O. Wunnicke, and P. Dederichs, Phys. Rev. B **66**, 024416 (2004).

[88] P. Weinberger, Phys. Rep. **377**, 281 (2003).

[89] O. Wunnicke, P. Mavropoulos, R. Zeller, and P. H. Dederichs, J. Phys.: Condens. Matter. **16**, 4643 (2004).

[90] O. Bengone, O. Eriksson, J. Fransson, I. Turek, J. Kudrnovský, and V. Drchal, Phys. Rev. B **70**, 035302 (2004).

[91] X. G. Zhang and W. H. Butler, Phys. Rev. B **70**, 172407 (2004).

[92] J. Mathon and A. Umerski, Phys. Rev. B **60**, 1117 (1999).

[93] S. Yuasa, T. Nagahama, A. Fukushima, Y. Suzuki, and K. Ando, Nature Materials **3**, 868 (2004).

[94] S. S. P. Parkin, C. Kaiser, A. Panchula, P. M. Rice, B. Hughes, M. Samant, and S. H. Yang, Nature Materials **3**, 862 (2004).

[95] S. Yuasa, A. Fukushima, H. Kubota, Y. Suzuki, and K. Ando, Appl. Phys. Lett. **89**, 042505 (2006).